# RELATIONSHIPS BETWEEN TSUNAMI SIZE AND EARTHQUAKE MAGNITUDE IMPROVED BY FAULT PARAMETERS

A THESIS SUBMITTED TO THE GRADUATE DIVISION OF THE
UNIVERSITY OF HAWAIʻI AT MĀNOA IN PARTIAL FULFILLMENT
OF THE REQUIREMENTS FOR THE DEGREE OF

MASTER OF SCIENCE

IN

OCEAN AND RESOURCES ENGINEERING

AUGUST 2020

By

Lin Sun

MS Committee:

Kwok Fai Cheung, Chairperson

Gerard J. Fryer

Yoshiki Yamazaki

Keywords: megathrust earthquake, tsunami, fault depth, fault dip, rigidity, wave shoaling

## Acknowledgments

First and foremost, I would like to express the most profound appreciation to my advisor Dr. Kwok Fai Cheung for the continuous and professional support of my M.S. study and research: he conveyed a stringent careful attitude in regard to research, and a spirit of exploration in scholarship. Without his guidance and help in either research or writing, this thesis would not have been possible.

Besides my advisor, I would like to thank the rest of my thesis committee: Dr. Gerard Fryer for the methodology and current procedures of tsunami warning, and Dr. Yoshiki Yamazaki for his guidance of NEOWAVE throughout my research and his previous work in tsunami modeling as an inspiration for my thesis.

In addition, I would like to extend my appreciation to Dr. Thorne Lay of the University of California Santa Cruz. His broad knowledge and acute insight on seismology were instrumental to my research. His summary and analysis of the recent submarine earthquakes have been an essential foundation for my thesis.

I would also like to thank some very family-like researchers: Dr. Linyan Li of OCEANIT and Dr. Ning Li. Their unrequited help at the early stage of my research and their enthusiasm for academics inspired me during my two-year master's study.

Last but not least, I would like to acknowledge, with gratitude, the support and love of my families - my parents: Zongzhe Sun and Yanqing Wu; my sister, Mingyue; my brother, Penghao; my second family: Jonathan, Steven, Terri, and Oliver Hargraves. They all keep me going and give me enormous support.

# Abstract

Megathrust earthquakes are the main source of tsunamis. The rupture at the plate interface deforms the seafloor, displacing seawater over a large region. The earthquake magnitude is not the only factor that affects the tsunami amplitude. A tsunami earthquake, which produces a much larger tsunami than what can be inferred from the seismic energy release, exemplifies this phenomenon. This thesis examines relationships between tsunami size and key geophysical attributes such as fault depth, fault dip, fault size, rigidity, and water depth, besides moment magnitude. The parametric study involves four sets of simplified megathrust-ocean models with an elastic planar-fault solution to define the earth surface deformation and a non-hydrostatic model to describe the resulting tsunami. The first set of models contains a flat seafloor to provide a baseline for comparison. The second set includes a flat seafloor abutting a 2° slope, and by varying the fault depth, fault dip, and water depth, explores the contributions from wave shoaling and wave energy anisotropy to peak tsunami amplitude. The third set utilizes the same topography to demonstrate effects of reduced rigidity or fault size for the same seismic moment. The fourth set examines the combined effects of the geophysical parameters as well as their trade-off. The results highlight the importance of depth-dependent fault rigidity and size in describing the two orders of magnitude variability in observed peak tsunami amplitude for given moment magnitude.

# Table of Contents

Acknowledgments ..... i
Abstract ..... ii
List of Tables ..... iv
List of Figures ..... v
1.Introduction ..... 1
2.Methodology ..... 6
*2.1. Seafloor Deformation* ..... 6
*2.2. Wave Model* ..... 7
*2.3. Models Setup* ..... 9
*2.4 Parametric Study* ..... 11
3.Results and Discussion ..... 15
*3.1 Tsunami Properties on Flat Seafloor* ..... 15
*3.2 Tsunami Properties on Slope* ..... 18
*3.3 Effects of Fault Width and Rigidity on Tsunami Properties* ..... 21
*3.4 Comparison with Recent Events* ..... 23
4.Conclusions and Recommendations ..... 27
References ..... 58

# List of Tables

Table 1. Interface-Rupture-Scaling Coefficients from Allen and Hayes (2017) ..... 10

Table 2. Parameters used as models inputs..... 12

# List of Figures

Figure 1. Geometry of planar fault model ..... 29

Figure 2. Sectional view of setup for NEOWAVE and planar fault model..... 29

Figure 3. Schematic of fault trimming from Allen and Hayes (2017) ..... 30

Figure 4. Seafloor vertical displacement from Model A as a function of dip angle and reference depth..... 31

Figure 5. Seafloor vertical displacement from Model A along fault centerline as a function of dip angle..... 32

Figure 6. Seafloor vertical displacement from Model A along fault centerline as a function of reference depth..... 33

Figure 7. Maximum uplift and subsidence from Model A as functions of dip angle and reference depth..... 34

Figure 8. Comparison of seafloor deformation and initial sea surface elevation for flat seafloor with 5000 m water depth..... 35

Figure 9. Comparison of seafloor deformation and initial sea surface elevation for a flat seafloor with 5000 m water depth..... 36

Figure 10. Peak surge and drawdown at the end of the rupture for Model A as functions of dip angle and reference depth for 5 km water depth..... 37

Figure 11. The ratio of Initial surge to uplift as a function of dip angle and reference depth. ..... 38

Figure 12. The ratio of Initial drawdown to subsidence as a function of dip angle and reference depth..... 39

Figure 13. The maximum sea surface elevation from Model A as a function of dip angle and reference depth for 5 km water depth ..... 40

Figure 14. The minimum sea surface elevation from Model A as a function of dip angle and reference depth for 5 km water depth ..... 41

Figure 15. Maximum surge and drawdown from Model A as functions of dip angle and reference depth for 5 km water depth. ..... 42

Figure 16. Seafloor displacement and sea surface elevation as functions of dip angle for 0 km reference fault depth and 5 km water depth. ..... 43

Figure 17. Seafloor displacement and sea surface elevation as functions of dip angle for 5 km reference fault depth and 5 km water depth. ..... 43

Figure 18. Maximum sea surface elevation from Model B as a function of dip angle and water depth for 0 km reference depth ..... 44

Figure 19. Minimum sea surface elevation from Model B as a function of dip angle and water depth for 0 km reference depth ..... 45

Figure 20. Maximum surge and drawdown from Model B as functions of dip angle and water depth for 0 km reference depth. ..... 46

Figure 21. Selected wave profiles at different time for 5 km water depth, 0 km reference depth and 5° dip angle ..... 47

Figure 22. Maximum surge and drawdown at shoreline from Model B as functions of dip angle and reference depth for 5 km water depth. ..... 48

Figure 23. Maximum surge and drawdown at shoreline from Model C as functions of dip angle for 5 km water depth and 0 reference depth. ..... 49

Figure 24. Maximum surge and drawdown at shoreline from Model C as functions of dip angle and rigidity for 5 km water depth and 0 reference depth. ..... 50

Figure 25. Maximum surge and drawdown at shoreline from Model C as functions of dip angle and slip distance for 5 km water depth and 0 reference depth. ..... 51

Figure 26. Log10 of the maximum sea reported surface elevation for 46 large interplate thrust earthquakes from 1990 considered in this study ..... 52

Figure 27. Comparison of computed peak surge from the wide fault and the recorded maximum sea surface elevation ..... 53

Figure 28. Maximum seafloor displacement and sea surface elevation as a function of *x* for moment magnitude ..... 54

Figure 29. Comparison of computed peak surge by from the narrow fault with various depth and the recorded maximum sea surface elevation ..... 55

Figure 30. Comparison of computed peak surge by from the narrow fault with various rigidity and the recorded maximum sea surface elevation ..... 56

Figure 31. Selected computed maximum surge from Figures 26, 28, 29 and the recorded maximum sea surface elevation as functions of earthquake moment magnitude ..... 57

# Chapter 1
# Introduction

Megathrust earthquakes are the primary source of tsunamis. Movement from slippage between continental and oceanic crusts causes uplift and subsidence of the seafloor, leading to large-scale displacement of seawater. The moment magnitude Mw is a measure of the seismic energy release and is often used as a criterion for tsunami hazard assessment, even though it does not necessarily have a direct relationship with the amplitude of the resulting tsunami. Other factors affecting seafloor deformation or tsunamigenic potential include the fault depth, fault dip, fault size, water depth, and rigidity. The most notable examples are tsunami earthquakes, which produce disproportionately large tsunamis for a given magnitude. Shallow rupture in the accretionary prism with low rigidity results in slow ground movement and weak shaking, but large seafloor displacement and hence large tsunamis (Kanamori, 1972).

The 1896 Sanriku tsunami earthquake was one of the most devastating, with 22,000 deaths in northeast Japan. The moderate ground shaking gave rise to 7.2 surface wave magnitude (Ms) and 8.0 moment magnitude (Mw), while the resulting run-up reached 38 m on the Sanriku coast with inferred tsunami magnitude Mt 8.2 and 8.6 from local and global data (Abe, 1979, 1981, 1994; Tanioka & Satake, 1996a; Tanioka et al., 1997). Comparison of recorded and computed tsunami travel times indicates the fault is very close to the toe of the continental margin and its eastern edge reached the trench at approximately 6 km water depth (Tanioka et al., 1997, Tsuru & Park, 2001). The 1946 Aleutian event is another representative tsunami earthquake. The shaking registered a moment magnitude of 7.4, but the resulting tsunami generated over 40 m of run-up at Scotch Cap immediately landward of the source with Mt 9.3 (Gutenberg & Richter, 1950; Johnson & Satake, 1997). The tsunami resulted in run-up reaching 13.7 m and took 159 lives in Hawaii, which is ~3,700 km away from the earthquake (Loomis, 1976). Okal & Hébert (2007)

inferred a triggering earthquake of Mw 8.6 from modeling of tsunami run-up observations in south Pacific islands.

A couple of well-studied recent events can illustrate the process and impact of tsunami earthquakes. The 25 October 2010 Mentawai, Indonesia Mw 7.8 earthquake originated at a depth of 12 km with an average slip of 6.5 m extending to the trench (Yue et al., 2014). Despite the low magnitude, the resulting tsunami generated run-up reaching 16.9 m at the small island of Sibigau and took 509 lives (Hill et al., 2012). The seismic waves with periods shorter than 100 s had low intensity. Residents felt only weak ground shaking and so did not evacuate. Weak ground shaking is a feature of tsunami earthquakes (Lay et al., 2011). The 17 July 2006 Java Mw 7.8 earthquake also excited a disproportionately large tsunami. Its run-up reached 8 m on the southern coast of Java and 21 m on the small island of Nusa Kambangan, with 802 lives lost (Fritz et al., 2007). Ammon et al. (2006) inferred from Rayleigh and body waves that the rupture had an unusually slow speed with a long duration and occurred near the up-dip edge of the subduction zone. The finite-fault models obtained for the 2010 Mentawai and 2006 Java events by Yue et al. (2014) and Ammon et al. (2006) confirm the extension of slip to the trench that is one of the important characteristics of tsunami earthquakes.

The 2011 Tohoku Mw 9.1 earthquake appeared to have a tsunami earthquake component (Yamazaki et al., 2018). The event ruptured the shallow part of the megathrust near Japan Trench and induced a tsunami with wave amplitude 5-6 m at the source and peak run-up of 40 m on the Sanriku coast (Fujii et al., 2011; Mori et al., 2011). Yamazaki et al. (2018) found the earthquake had a peak slip of 56 m located up-dip of the hypocenter at 10-30 km from the trench and another significant slip patch of 20 m average at the northern rupture zone off the Sanriku coast along the trench. This epicentral slip is consistent with seafloor GPS measurements and other published fault models based on seismic and tsunami measurements, but the rupture to the north

is not resolvable from the seismic record and only inferred by a handful of models that include tsunami observations (Lay, 2018). The northern near-trench slip, which is needed to explain the 40 m run-up on the Sanriku coast, suggests re-rupture of the 1896 Sanriku tsunami earthquake region during the 2011 event with significant implications for tsunami hazard assessment.

The near-trench rupture with low rigidity provides an explanation for low magnitude tsunami earthquakes (Kanamori, 1972). The large observed tsunami run-up might also be attributed to wave shoaling over the continental margin from the deep trench. Tsunamis are mostly shallow-water waves with the celerity and group velocity given by $c=c_g=\sqrt{gh}$, where $h$ is water depth, and $g$ is the acceleration due to gravity. As waves propagate up-slope from $h_0$ to $h_1$, the shoaling coefficient from linear wave theory and an assumption of gentle seafloor slope is

$$K_S=\sqrt{\frac{c_{g0}}{c_{g1}}}=\left(\frac{h_0}{h_1}\right)^{\frac{1}{4}} \tag{1}$$

where $c_{g0}$ and $c_{g1}$ are evaluated at $h_0$ and $h_1$. The shoaling coefficient, which provides a first-order estimate of the wave amplitude ratio between the two locations, shows the observed wave amplitude near shore has a positive relationship with the source water depth $h_0$. A tsunami generated near the trench will have a greater increase in amplitude at the shore. The shoaling effect becomes more prominent if wave nonlinearity is taken into consideration (USACE, 2006).

In tsunami warning, earthquake moment magnitude is initially calculated using the Mwp algorithm (Tsuboi et al., 1995). The Mwp method takes the first ~20 seconds of the P-waves recorded at each seismometer, integrates twice to convert velocity to moment, then picks the peak in the resulting trace of moment versus time to get an approximate Mw for the earthquake. The magnitude determination is automated, stable, and takes about six minutes, though results are available faster if there are more seismic stations near the source. For earthquakes occurring

within the Hawaiian Islands, the Pacific Tsunami Warning Center (PTWC) will issue a warning statement for any shallow coastal or offshore earthquake exceeding magnitude 6.9 (https://www.tsunami.gov). Because the islands are well instrumented, PTWC will issue any necessary warning within three minutes of the earthquake origin time.

While fast, Mwp is only very approximate. Warning centers and seismic observatories therefore automatically trigger the W-phase source determination (Kanamori, 1993; Kanamori & Rivera, 2008), for all earthquakes greater than magnitude 6. The W-phase method looks at multiply-reflected seismic body waves at periods longer than 100 seconds to compute both the moment magnitude and a centroid moment tensor. As presently implemented, the W-phase source determination takes about 25 minutes due to the need of data from a broad range of azimuths and distances. Incorporating geodetic data from near-source GPS receivers will soon reduce that time to <10 min (Lay et al., 2019; Kaneko et al., 2010; Segall & Davis, 1997; Blewitt et al., 2006; Allen & Ziv, 2011).

The Pacific Tsunami Warning Center routinely forecasts tsunamis using RIFT (Wang et al., 2012), a real-time forecast model based on linear shallow-water theory, and the source defined by the W-phase CMT (if the CMT is not yet available, RIFT is run for an assumed mechanism using Mwp). For most events, the RIFT results are within a factor 2 of DART observations and the run time is only a few minutes (Wang et al., 2017). The initial rigidity used in RIFT is 45 GPa, but for earthquakes with slow rupture, the rigidity is dropped to about 20 GPa. Slow rupture can be detected from the slowness parameter, which compares high-frequency body-wave energy to the seismic moment (Weinstein & Okal, 2005).

It is still very challenging to rapidly quantify the fault geometry, slip distribution, and dip angle for rapid tsunami warning (Titov et al., 2005; Lay et al., 2019). Because the various parameters of the earthquake jointly affect the amplitude of the tsunami, there is a need for quantitative

analysis of the effects of the individual parameters. Understanding the roles of key geophysical parameters on tsunami wave amplitude will help improve tsunami-warning protocols, interpretation of earthquake and tsunami records as well as inversion analysis of megathrust earthquakes.

This research utilizes a planar-fault model of earthquakes and the non-hydrostatic tsunami code NEOWAVE of Yamazaki et al. (2009, 2011) to examine relationships between the maximum tsunami wave amplitude with key parameters such as fault depth, fault dip, fault size, and rigidity, beside the moment magnitude. NEOWAVE, which accounts for nonlinearity, can provide a realistic description of wave transformation processes over the upper plate seafloor slope. Section 2 summarizes the methodology that includes modeling of seafloor deformation and tsunami propagation from earthquake faulting as well as the design of the parametric study. Chapter 3 includes the model results from the parametric study, discussions of the role of each parameter in the peak tsunami amplitude, a comparison with the recent interplate earthquake and tsunami records. This is followed by the conclusions and recommendations in Chapter 4. Finding the main factors that determine the tsunami size can improve the accuracy of real-time tsunami warning and reduce the human and economic losses caused by the tsunami.

# Chapter 2

# Methodology

This section describes seafloor displacement due to slippage of a planar fault in an elastic half-space and the depth-integrated governing equations for modeling of the resulting non-hydrostatic flow. Tsunami modeling includes two important aspects: generation and propagation. It is generally accepted that tsunami generated by seafloor displacement are affected by the fault size and slip and to a certain extent the rise time. Okada (1985) gives a solution for the seafloor deformation from slippage of a planar fault. The seafloor deformation produces a positive and a negative sea surface pulse, which under gravitational force, oscillate and spread in the horizontal direction as a series of waves. The depth-integrated, non-hydrostatic model of Yamazaki et al. (2009, 2011) is used to describe the wave generation and propagation. The vertical velocity from the moving seafloor is applied to describe the generation of the tsunami.

## *2.1. Seafloor Deformation*

The seafloor deformation from earthquake rupture can be computed analytically using dislocation theory. Consider a homogeneous and elastic half space in three dimensions. Steketee (1958) defined the displacement field $\eta_i(x_1, x_2, x_3)$ due to a dislocation $\Delta\eta_j(\xi_1, \xi_2, \xi_3)$ across a surface S as

$$\eta_i = \frac{1}{F}\iint_{\Sigma} \Delta\eta_j \left[\lambda\delta_{jk}\frac{\partial\eta_i^n}{\partial\xi_n} + \mu\left(\frac{\partial\eta_i^j}{\partial\xi_k} + \frac{\partial\eta_i^k}{\partial\xi_j}\right)\right] v_k dS \tag{2}$$

where $\delta_{jk}$ is the Kronecker delta, $\lambda$ and $\mu$ are Lame's constant, and $v_k$ is the direction cosine of the normal to the infinitesimal surface $dS$ with the summation convention. The displacement $\eta_i^j$ is the $i^{th}$ component at the field point $(x_1, x_2, x_3)$ due to dislocation in the $j^{th}$ direction at the source point $(\xi_1, \xi_2, \xi_3)$.

Okada (1985) derived the solution of equation (2) for a planar fault of length L and width W in a Cartesian coordinate system (*x*, *y*, *z*) that has been used as a standard for computation of earth surface deformation from earthquake rupture. As illustrated in Figure 1, the fault plan is defined by the reference depth, strike angle, and dip angle and ($\eta_1$, $\eta_2$, $\eta_3$) denotes the earth surface displacement in the *x*, *y*, and *z* directions. The planar-fault dislocation is denoted by the slip and the rake angle. The vertical component of the seafloor displacement due to earthquake rupture is the primary excitation in tsunami generation (Kajiura & Rivera, 1981). If an earthquake happens beneath the continental slope, the horizontal displacement also introduces a vertical motion of the seafloor. The laboratory study of Iwasaki (1982) shows that a tsunami generated by the horizontal displacement is significant if the seafloor slope is greater than 1/3. Tanioka and Satake (1996b) derived a simple geometric correction to the vertical displacement of the seafloor to account for horizontal displacement on a slope.

### *2.2. Wave Model*

NEOWAVE (Non-hydrostatic Evolution of Ocean WAVEs) is a community model for computation of tsunami generation, propagation, and inundation in a single calculation without external transfer of data (Yamazaki et al., 2009; 2011). The model has been benchmarked by the National Tsunami Hazard Mitigation Program for mapping of coastal inundation and currents (Yamazaki et al., 2012; Bai et al., 2015). The formulation includes the non-hydrostatic terms for modeling of tsunami generation and wave dispersion. Cartesian coordinates are used for tsunami modeling in this thesis because the maximum wave amplitude occurs near the source and the curvature of the earth is negligible. Let t denote time and n is the Manning's roughness coefficient with a default value of 0.025. The governing equations describe conservation of momentum in the *x*, *y*, and *z* directions as well as flow continuity in the *x*-*y* plane as

$$\frac{\partial U}{\partial t} + U\frac{\partial U}{\partial x} + V\frac{\partial U}{\partial y} = -g\frac{\partial \zeta}{\partial x} - \frac{\partial Q}{\partial x} - \frac{Q}{D}\frac{\partial(\zeta - h)}{\partial x} - n^2\frac{g}{D^{1/3}}\frac{U\sqrt{U^2+V^2}}{D} \tag{3}$$

$$\frac{\partial V}{\partial t} + U\frac{\partial V}{\partial x} + V\frac{\partial V}{\partial y} = -g\frac{\partial \zeta}{\partial y} - \frac{\partial Q}{\partial y} - \frac{Q}{D}\frac{\partial(\zeta - h)}{\partial y} - n^2\frac{g}{D^{1/3}}\frac{U\sqrt{U^2+V^2}}{D} \tag{4}$$

$$\frac{\partial W}{\partial t} + U\frac{\partial W}{\partial x} + V\frac{\partial W}{\partial y} = \frac{2Q}{D} \tag{5}$$

$$\frac{\partial \zeta}{\partial t} + \frac{\partial UD}{\partial x} + \frac{\partial VD}{\partial y} = 0 \tag{6}$$

in which ($U$, $V$, $W$) is the depth-averaged velocity, $\zeta$ is the water surface elevation, $Q$ denotes the depth-averaged non-hydrostatic pressure, and $D = \zeta + h - \eta$ is the flow depth, where $h$ is the water depth and $\eta$ is the vertical seafloor displacement. Tanioka and Satake (1996b) give

$$\eta = \eta_z + \frac{\partial h}{\partial x}\eta_x + \frac{\partial h}{\partial y}\eta_y \tag{7}$$

where the second and third terms on the right-hand side account for the contribution of the horizontal seafloor displacement on a slope.

The non-hydrostatic model utilizes the vertical velocity component $W$ to describe wave dispersion. The tsunami can be generated by a static initial waveform or dynamically through the seafloor vertical displacement over a prescribed rise time. The latter generation mechanism transfers both kinetic and potential energy from vertical displacement of the seafloor to the water. NEOWAVE accounts for momentum transfer from the vertical to the horizontal direction during seafloor excitation and describes propagation of tsunami waves away from the source simultaneously. This might results in a waveform at the end of the rupture different from the static seafloor displacement (e.g., Li et al., 2016).

*2.3. Models Setup*

A simplified ocean-megathrust model is utilized to investigate the influence of fault dip, fault depth, fault size, water depth, and rigidity on the peak tsunami wave amplitude. Figure 2 provides a sectional view of the model setup with the planar fault solution and NEOWAVE. The x-axis is along the model centerline pointing toward the subduction zone and its origin is directly above the upper edge of the plate interface, while the z-axis is pointing upward from the initial sea surface. The y-axis, which is not shown in the figure, is along the upper edge of the fault plane pointing into the page. The rectangular fault with length L and width W is set on the plat interface with its upper edge is along the trench. The reference depth *d* is defined as the vertical distance from the original seafloor to the upper edge of the fault. The water depth $h_0$ is measured from the initial sea surface to the abyssal plain to distinguish the water depth h, which is a function of x. The vertical seafloor displacement $\eta$ is defined by equation (7) and $\zeta$ is the sea surface elevation generated by the seafloor displacement as a function of time.

Allen and Hayes (2017) provide rupture-scaling relationships for fault length and width as functions of Mw for subduction earthquakes (Table 1). The relationships are based on more than 160 finite fault models of earthquakes since 1990 and source models of the 1952 Kamchatka Mw 8.9, the 1957 Aleutian Islands Mw 8.6, the 1960 Concepcion Mw 9.5, and the 1964 Prince William Sound Mw 9.3 earthquakes before 1990. In the scaling relationships, the fault width is saturated at 196 km when earthquakes are greater than Mw 8.6, because the physical characteristics of the subduction zone limit the depth range of the rupture. The finite fault models, which were determined from seismic wave inversion, depict non-uniform and sometimes complex distributions of slip (Hayes et al., 2015). Although Allen and Hayes (2017) remove sub-faults whose slip is less than 15% of the maximum, due to the irregularity of the actual fault geometry, when a rectangular area is used to represent the fault, it is inevitable to

include sub-faults which are outside of the actual fault as illustrated in Figure 3. Compared with the primary earthquake scaling relationship from Wells and Coppersmith (1994), Allen and Hayes (2017) might underestimate the average slip and overestimate the fault width. Brengman et al. (2019) find that the scaling relationships from Allen and Hayes (2017) might be poorly constrained due to the small magnitude range in the database used and multiple regressions can fit the data range equally well. Compared with the fault scaling relationships developed by Brengman et al. (2019), Allen and Hayes (2017) might underestimate the down-dip fault size. Therefore, the scaling relations represent the average conditions from a dataset of limited size to provide a reference or baseline for comparison. Numerous studies on finite fault inversion of seismic events show that the majority of slip is concentrated in sub-faults over a much smaller area (Yamazaki et al., 2018, Ye et al., 2016, Fuentes et al., 2016, Newman et al., 2011, Ammon et al., 2006). Considering the sensitivity of a tsunami to fault slip, it is necessary to consider the trade-off between fault slip and size.

Table 1. Interface-Rupture-Scaling Coefficients from Allen and Hayes (2017)

| Function | a | b | Condition* |
|---|---|---|---|
| $\log L\ (km) = a + b \times Mw$ | -2.90 | 0.63 | - |
| $\log W\ (km) = a + b \times Mw$ | -1.91 | 0.48 | $Mw \leq 8.67$ |
| | 2.29 | 0.00 | $Mw \geq 8.67$ |

* All interface relationships are valid from $7.1 \leq Mw \leq 9.5$.

The scaling relations of Allen and Hayes (2017) provide the fault dimensions L and W as functions of the moment magnitude, which is related to the seismic moment $M_0$ by Kanamori (1977) as

$$M_w = \frac{2}{3}\log M_0 - 6.03 \tag{8}$$

The slip is computed from the seismic moment from Aki (1966)

$$\mathrm{M_0} = \mathrm{G\,A\,S} \tag{9}$$

where G is rigidity (shear modulus), $A = L \times W$ is the rupture area, and S is the average slip during rupture. The rigidity, which depends on the rock layer and depth, has a range from 20 to 75 GPa in the Preliminary Reference Earth Model (PREM). Bilek & Lay (1999), however, suggest a much wider range inferred from the stress drops in 291 earthquake events.

*2.4 Parametric Study*

The key parameters influencing tsunami amplitude include the reference depth *d*, water depth *h*, dip angle δ, and the earthquake magnitude, which in turn determines the fault dimensions and slip. With the strike and rake angles assumed to be 0° and 90°, each rupture scenario is described by a planar fault in terms of the reference depth, dip angle, fault dimensions, and slip. The rupture is assumed to occur simultaneously across the fault plane with a rise time of 15 sec for modeling of tsunami generation. Since tsunami waves have a much longer period, the rise time within its typical range has negligible effects on the resulting tsunami (Li et al., 2016). The model settings are divided into Suites A, B, C, and D to examine effects of individual parameters on the tsunami wave amplitude as well as their interplay.

Table 2 provides an overview of the parameters used for all models. The NEOWAVE domain has a rectangular planform and its cross-section at its centerline is illustrated in Figure 2. The domain is 1000 km by 800 km in the x and y directions for earthquakes with Mw < 9.5 and 1000 km x 1600 km for earthquakes with Mw 9.5. A 1-km grid size is sufficient to resolve tsunami waves over flat bottom, and a 500-m grid is used, when a bottom slope bottom is involved, to better account for wave shoaling and reflection from landmass. All model suites cover the dip

angle from 5 to 25°. Suite A simulates earthquakes underneath a flat seafloor with θ = 0°, while varying the fault dip and depth in turn to examines their influence on tsunamigenic potential. A water depth of 5 km is typical at oceanic trenches, where most tsunamigenic earthquakes occur. The fault width and length are determined from Allen and Hayes to be 85 km and 138 km for the Mw 8.0 earthquake. The seismic moment of $1.26\times10^{21}$ Nm and 40 GPa rigidity give 1.34 m average slip. The results for a flat seafloor provide a baseline and a reference for comparison.

Suite B simulates earthquakes, which ruptures the shallow part of a subduction zone during a megathrust event. The seafloor deformation for the Mw 8.0 earthquake remains the same for the given reference depth of 0 km as in Suite A. A range of water depths is utilized to explore the contributions from wave shoaling over the upper plate slope and reflection from landmass. The slope is set at 2°, since wave shoaling is generally independent of the gentle slope typical of most continental margins. The planar fault solution of Okada (1985) is based on a half space, the effective dip angle including the seafloor slope is used in the computation of seafloor deformation. Suite C models are set to demonstrate the effects of fault width and rigidity. The narrow fault is defined as having half of the width from Allen and Hayes (2017) and twice the slip for the same seismic moment. Rigidity with 40 GPa is typical but not suitable for shallow-rupture earthquake. The slip increases further by a factor ranging from 4 to 8 to compare with Suite A and B by decreasing the rigidly from 40 to 10 GPa.

Table 2. Parameters used as models inputs

| Model | Mw | Rigidity | Fault | Ref. Dep. (km) | Dip Angles (°) | Water depth |
|---|---|---|---|---|---|---|
| A | 8.0 | 40 | Wide | 0, 5, 10, 15, 20 | 5, 10, 15, 20, 25 | 5 km uniform |
| B | 8.0 | 40 | Wide | 0 | 5, 10, 15, 20, 25 | 3, 4, 5, 6 km with 2° slope |
| C1 | 8.0 | 40 | Narrow, Wide | 0 | 5, 10, 15, 20, 25 | 5 km with 2° slope |

| | | | | | | |
|---|---|---|---|---|---|---|
| C2 | 8.0 | 10, 20, 30, 40 | Narrow | 0 | 5, 10, 15, 20, 25 | 5 km with 2° slope |
| D1 | 7.0, 7.5, 8.0, 8.5, 9.0, 9.5 | 40 | Wide | 0, 5, 10, 15, 20 | 5, 10, 15, 20,25 | 5 km with 2° slope |
| D2 | 7.0, 7.5, 8.0, 8.5, 9.0, 9.5 | 40 | Narrow | 0, 5, 10, 15, 20 | 5, 10, 15, 20,25 | 5 km with 2° slope |
| D3 | 7.0, 7.5, 8.0, 8.5, 9.0, 9.5 | 5, 10, 20 | Narrow* | 0 | 5-25** | 5 km with 2° slope |

*The rigidity reverts to 40 GPa below 15 km from the sea surface according to Lay et al. (2012)

**Computation to identify the maximum sea surface elevation within the range of dip angle

The models in Suite D examine the interplay between rigidity, fault width, and reference depth as well as the scaling with earthquake magnitude for comparison with historical records. The seafloor slope and water depth are fixed at representative values of 2° and 5 km, respectively. The rigidity is 40 GPa in Suites D1 and D2, in which the reference depth is varied to explore its effects on tsunami size. Decreasing the rigidity down to 5 GPa in Suite D3 can describe the shallow slip earthquakes in the limiting conditions. Lay et al. (2012) give an estimate of average source region rigidity as a function of the source depth. Rigidity of 5 GPa mostly exists less than ~10 km from the sea surface. As the source depth increases to 15 km, the rigidity increases approximately linearly to ~20 GPa. Rigidity in depths from 15 to 30 km below the sea surface is in a range of 20 to 40 GPa. The rigidity of 5 to 20 GPa is not applicable to deep rupture, so the value is reverted to 40 GPa below 15 km from the sea surface while the seismic moment remains uniform over the fault.

The earthquake magnitude ranges from 7.0 to 9.5 for most cases in Suites C, D1, D2, and D3, except for cases with large reference depths or low rigidity, in which the earthquake magnitude is capped at 8.0 or 8.5. This is because the fault depth limits the earthquake magnitude. Large earthquake magnitude is not suitable for cases with rigidity of 5 GPa either, as such low rigidity

only exists in the shallowest part of a fault and typically do not contribute to seismic events greater than Mw 8.0 (Lay et al., 2012).

# Chapter 3
# Results and Discussion

The parametric study of megathrust earthquake and tsunami properties is divided into four stages. The first stage utilizes an Mw 8.0 earthquake underneath a flat seafloor, and by changing the dip and reference depth, studies their roles in generation of a tsunami. Secondly, the flat seafloor is connected to a two-degree slope to examine shoaling of the tsunami with water depths from 3 km to 6 km and reference depths from 0 km to 10 km. Thirdly, by keeping the Mw at 8.0 and varying the slip according to Equation (9), the effects of fault width and rigidity are studied. Lastly, the peak tsunami amplitude is computed as a function of earthquake magnitude along with ranges of fault parameters to identify the best match with records from historical events.

## *3.1 Tsunami Properties on Flat Seafloor*

The main cause of tsunamis is underwater earthquakes, primarily from dip-slip faults, characterized by the vertical displacement component of the motion along the fault plane. Large-scale changes in the seafloor displace water and generate tsunamis. The main factors affecting the tsunamis are the magnitude of the earthquake, the faulting mechanism, and the depth of the source. In Model A, the seafloor is simplified as flat to eliminate effects of wave shoaling and with a Mw 8.0 earthquake and 5 km water depth, the effects of dip angle and fault depth on seafloor deformation and tsunami generation are studied.

The seafloor deformation, as shown in Figure 4, includes uplift over most of the fault and subsidence toward the downdip end and beyond. The deformation is maximum along the centerline and is rather uniform over the length with rapid attenuation on the two sides. Figures 5 and 6 provide the deformation profiles arranged to highlight the effects of the dip angle and reference depth respectively. The uplift is discontinuous when the fault reaches the seafloor, and is equal to the vertical component of the slip motion. With the reference depth slightly increased

from 0 to 5 km, the discontinuity disappears, and a pointed uplift patch appears instead. The peak uplift is larger than the vertical component of the slip motion due to elastic deformation created by the entire fault. With the reference depth increased from 5 to 25 km, the uplift patch widens and the vertical displacement varies with a factor of 3.4 for dip angle of 5° and a factor of 1.3 for dip angle of 25°. The peak subsidence is not sensitive to the range of reference depths considered, while the deformation field becomes more gradual and spread out with increasing reference depth. When the dip angle and reference depth are small, the uplift and subsidence are more localized due to proximity to the seafloor consistent with St. Venant's Principle (1856).

Figure 7 summarizes the peak uplift and subsidence as functions of the dip angle and reference depth. The uplift increases with the dip angle due to the larger vertical component of the slip motion, while the subsidence is shallower with larger dip angles due to the deeper downdip end of the fault. Conversely, the reference depth has a greater influence on the uplift due to greater proximity of the updip end of the fault to the seafloor. The peak uplift is identical to the vertical component of the fault motion when the fault pierces the seafloor. The uplift increases sharply when the fault is just below the seafloor due to the large elastic deformation that should otherwise be a crack. The artifact quickly attenuates with increasing reference depth as the deformation can largely be described by the elastic half-space model.

The dynamic seafloor displacement transfers potential and kinetic energy into the water, which generates a tsunami. Figures 8 and 9 compare the seafloor deformation and sea surface elevation at the end of the rise time, which lasts 15s in the models. When the reference depth is zero, the abrupt uplift generates a rarefaction on the main pulse and a transient shock that transitions into a secondary wave across the discontinuity. Since the uplift patch is width compared to the water depth, the surface pulse has a very similar amplitude as the uplift despite the rarefaction. The localized subsidence results in a shallower and wider negative pulse at the surface. At 5 km reference depth, the narrow uplift produces a wider sea surface pulse with smaller amplitude due

to spreading of the seafloor excitation over the water column. Such effects diminish with increasing reference depth as the seafloor deformation becomes gentler.

The attenuation of the seafloor excitation to the sea surface is of particular interest for tsunami modeling. Figure 10 shows the maximum and minimum sea surface elevations at the end of the rupture. The initial surge is affected by the shape of uplift, while the drawdown is not as sensitive to the subsidence or the fault reference depth. Figures 11 and 12 show the ratios of the initial sea surface elevation to the seafloor displacement at the peak uplift and subsidence. For surface-piercing faults, the ratio for the surge is close to one for small dip angles due to the rather uniform uplift above most of the fault. The gradual decrease with increasing dip angle reflects the declining uplift in the downdip direction associated with a deeper lower edge of the fault. The ratio decreases dramatically from 0 to 5 km reference depth due to the pointed narrow uplift patch and reduced effectiveness in pushing the water up. For buried faults, the width of the uplift patch and consequently the ratio with the surge increase with the dip angle and reference depth. The subsidence generally gets shallower and wider with increasing dip angle and reference depth. The ratio with the sea surface drawdown has a more monotonic increasing trend with the dip angle and reference depth.

With the seafloor excitation defined, the computation continues for one hour of elapsed time to fully develop the tsunami flow in the domain. Figures 13 and 14 provide examples of the computed maximum and minimum sea surface elevations. The maximum sea surface elevation generally occurs above the maximum uplift for flat bottom, except for the model with 5° dip angle and 0 km reference depth, in which the maximum sea surface elevation occurs about 192 km away from the maximum uplift due to constructive interference of the waves generated by the uplift and subsidence. For 5° dip angle, the maximum drawdown is caused by deep subsidence. When the dip angle is relatively large (10° - 25°), the subsidence is small and the maximum drawdown is generated near the maximum uplift due to free surface oscillations generated by the large initial positive pulse.

Figure 15 shows the maximum surge and drawdown from Model A as a function of dip angle and reference depth. The results closely correspond to those at the end of the rupture in Figure 10, with a few exceptions when the constructive interference of the waves from the uplift and subsidence produces augment the initial surge. Compared the maximum surge in Figure 15 with the maximum uplift in Figure 7, it can be seen that a larger uplift peak does not always give a larger initial sea surface displacement. For example, a fault with 5 km reference depth generates a larger uplift peak but a smaller tsunami in comparison to the fault with a 10 km reference depth. The shallower fault produces steeper uplift, which is less effective in pushing the water up. Even when static initial conditions are used, Satake et al. (2017) indicate that tsunami heights are larger for deeper subfault of 3.5 - 7 km than for shallower subfaults of 0 to 3.5 km in modeling of the 1896 Sanriku earthquake. The sensitivity of the maximum surge to reference depth becomes weaker with increasing depth and dip, which can be explained by St. Venant's (1856) Principle and the change in the vertical component of fault slip. Generally, the maximum surge increases and then decreases with the reference depth due to the change in both the uplift peak and width. The shape of deformation dominates the initial wave amplitude, and there exists an optimal reference depth (which is 15 km in the Model Suite A) when the deformation is most efficient at displacing water. Large sea surface drawdowns occur at two locations during the tsunami generation. One occurs simultaneously with the seismic activity by the subsidence. The second is caused by the descending initial pulse after the seismic activity ends. As the dip angle increases, the peak value of subsidence decreases significantly, and the maximum drawdown shifts from the fault's lower edge to its upper edge.

### *3.2 Tsunami Properties on Slope*

The modeling with a flat seafloor has established a baseline for investigation of wave transformation on a 2° slope representative of the upper plate through Model Suite B. The earthquake magnitude remains at 8.0 in this series of tests. The reference depth is measured from

the sloping seafloor and the dip angle from the horizontal portion of the seafloor as shown in Figure 2. The seafloor slope effectively increases the dip angle. Besides the uplift, the subsidence also contributes to the initial wave, especially for models with small dip angles which generate large subsidence. Figures 16 and 17 show the seafloor deformation and surface elevation at the end of the rupture in terms of the dip angle for reference depths of 0 km and 5 km respectively. The rupture produces an initial surge updip and drawdown adjacent to the shore. The horizontal motion of the sloping seafloor in the offshore direction augments the surge, while reducing the drawdown.

Both wave shoaling and interaction on the slope depend on the water depth. Figures 18 and 19 show the maximum and minimum surface elevations over the computational domain for 4, 5, and 6 km water depth at the abyssal plain. The peak surge and drawdown occur at the shoreline. The increase in water depth extends the width of the slope and enhances the maximum surge. The complete set of results in Figure 20 shows the same pattern. This is consistent with the shoaling coefficient in Equation (1), which indicates an increase in near-shore wave amplitude with the water depth at the initial wave. Besides, an increase of the water depth should enhance wave propagation toward the shore. In shallow water, the dispersion relation is expressed as

$$c = \sqrt{gh} \tag{10}$$

in which

$$h = h_o - x\tan(\theta) \tag{11}$$

where $h_o$ is the water depth at the abyssal plain and is the seafloor slope (see Figure 2). The gradient of the celerity is given by

$$\frac{dc}{dx} = \frac{d\sqrt{gh}}{dx} = \frac{d\sqrt{g(h_o - x\tan(\theta)}}{dx} = -\frac{\sqrt{g}\tan\theta}{2\sqrt{(h_o - x\tan(\theta))}} \tag{12}$$

As the water depth $h_0$ increases, the gradient of the celerity decreases and more energy from the initial pulse propagates toward the shore. Both the shoaling process and celerity gradient elucidate the reason that the surge at the shore increases with the water depth..

The time series of the surface elevation are analyzed to understand the interaction between the waves generated by the initial surge and drawdown . Figure 21 shows the time histories of the incident and reflected waves with $h_0$ = 5 km and 5° dip angle. The trough of the incident wave arrives at the shore inducing a drawdown at 13 min 30 sec, and then the water surface rebounds and runs up on the slope. Meanwhile, the crest of the initial wave arrives at 15 min 39 sec, and the run-up from the combined energy reaches the maximum at 17 min 6 sec. During the drawdown on the slope, it can be clearly seen that the trough of the initial wave becomes a peak of the reflected wave and the crest of the initial wave becomes a trough. Whether the trough and crest can be superimposed to strengthen the surge at the shore depends on the wavelength and period. The wavelength relates to the fault width as a function of Mw, and the period can be expressed as the wavelength divided by the celerity where the tsunami was generated. In addition, the increase in water depth decreases the initial wave at the end of rupture process, but this effect only contributes to at most 3% of the surge or drawdown at the shore and is negligible.

Figure 22 plots the maximum surge and drawdown on the slope as a function of dip angle and reference depth. The surge is the highest when the reference depth is zero and the dip angle is large as the fault is located furthest from land and the seafloor deformation occurs at deeper water. By increasing the reference depth or decreasing the dip angle on dipping bottom, the fault move towards to the shore. Once part of the fault is close to or below dry land, there is less energy for the tsunami generation.  An increase in dip angle or reference depth contributes to the depth of the fault's lower edge and reduces the subsidence. The subsidence appears to play a minor role in the drawdown, which actually increases with these two parameters.

The dipping seafloor simply mimics the role of upper plate slopes in the process of tsunami generation and shoaling. The water depth and the seafloor slope affect the amount of energy propagation on and offshore. Shoaling is enhanced with an increase of water depth. An important finding is that the negative pulse generated by subsidence may be reflected as a positive pulse with considerable contribution to the surge at the shore. Rupture of deep faults beneath dry land, explains why the 2012 Costa Rica earthquake with considerable magnitude, produced an extremely small tsunami (Liu et al., 2015).

### *3.3 Effects of Fault Width and Rigidity on Tsunami Properties*

The fault size in Models A and B is calculated from the rupture-scaling relationship of Allen and Hayes (2017) and is representative of an average rupture area, instead of the most tsunamigenic peak slip region. In addition, the rigidity of 40 GPa is on the high side of the range suggested by Lay et al. (2012) for shallow faulting. The variation of fault size and rigidity alters the slip for the same seismic moment and subsequently tsunami amplitude. In Model Suite C, two series of tests are used to evaluate the effect of fault width and rigidity on tsunami amplitude.

Model C1 has a reference depth of 0 km, and the rigidity is held at 40 GPa with a given Mw 8.0. Setting the potency ($A \times S$) as constant allows adjustment of the rupture area or slip to modify the seafloor deformation while maintaining the same seismic moment. The fault width of 83 km obtained from Allen and Hayes (2017) provides a reference. A test with the fault width reduced by half and the slip doubled examines the interplay between the two parameters for the same Mw 8.0. The resulting fault dimensions of 42.5 km by 138 km are close to what has been postulated for the 1896 Sanriku earthquake (Tanioka et al., 1996a).

Figure 23 shows the results of Model C1. As the fault width is halved and the slip is doubled, the maximum surge is approximately doubled. Shortening the width of the fault decreases the wavelength and places the initial tsunami wave at a larger average water depth to increase the

shoaling coefficient. In addition, the lower edge of the fault at a shallower depth beneath the seafloor enhances the subsidence. The effects become more pronounced for large dip angles with more than 100% increase of the peak surge from the reference case. Although the maximum drawdown increases with the increase of slip caused by the narrowing of the fault width, it is not as prominent as the maximum surge. This may be explained by the nonlinear Cnoidal wave theory for shallow-water waves. While the crest has a direct relationship with the wave height, the trough is controlled nonlinearly by the wave height and wavelength. The larger wave height and shorter wavelength from the narrow fault result in a slight increase of the trough depth and consequently the drawdown at the shore in comparison to the reference.

The rigidity of 40 GPa might be high for the shallow, trench piercing slip. To find a reasonable value for faults with different depth, Bilek & Lay (1999) and Lay et al. (2012) provide a relationship between rigidity and fault depth. Generally, increasing in fault depth leads to an increase in rigidity, and the small rigidity only exists at depths of less than 15 km from the sea surface. Model C2 keeps the model setup with a narrow fault as in Model C1. The rigidity is reduced from 40 to 30, 20, and 10 GPa in turn with corresponding slip increased to maintain the same Mw 8.0. When compared to the wide fault from Allen and Hayes (2017), the slip increased by a factor of up to 8 in model set C2. Figure 24 shows that lower rigidity and larger dip angle produce larger tsunamis. Decreasing the rigidity leads to an increase of slip for a given Mw. The result shown in Figure 25 indicates that the tsunami size is nearly proportional to the slip for an earthquakes with the same fault size. The slip change caused by the change of fault size or rigidity is a more direct factor that affects tsunami size. The fault width and rigidity affect the tsunami wave amplitude through the amount of slip and the subsequent seafloor deformation from Okada (1986). Low rigidity results in a larger tsunami for the same moment magnitude. This result is consistent with the observations of Kanamori (1972) that the tsunami earthquake, which produces unexpectedly large tsunami for its seismic moment, occurred at shallow depth with low rigidity. Model C indicates that earthquakes of the same moment magnitude may

generate tsunamis with a broad range of amplitude due to the amount of slip caused by the different fault sizes and rigidity. This is also one of the reasons why the method of using only the earthquake magnitude to predict the tsunami size is quick but not reliable.

### *3.4 Comparison with Recent Events*

Issuance of tsunami warnings is usually based on a limited amount of information obtained within a short period of time after a submarine earthquake. At present, the available information includes the earthquake intensity calculated from the initial P- and S-wave seismic signals, Deep-ocean Assessment and Reporting of Tsunami (DART) data as well as real-time GPS observations (Titov et al., 2016, Huang et al., 2017). Those data can be obtained within a short period of time, but lacks resolution to fully define the fault geometry for detailed tsunami modeling.

Lay et al. (2019) considered the maximum sea surface elevations and Mw for 52 interplate thrust events from the NOAA Global Historical Tsunami Database (https://www.ngdc.noaa.gov/hazard/tsu_db.shtml) and estimated whether the rupture has at least some slip at shallow depth for each event. The maximum tsunami amplitude of the events includes a combination of local run-up, tide gauge measurements, and pressure sensor observations. The compiled data in Figure 26 illustrates that seismic events with the same Mw can generate tsunamis with peak amplitudes of up to two orders of magnitude variability. The size of a tsunami is not a unique function of Mw. Other seismic parameters, like fault depth and fault size, and mantle physical properties are also responsible for the tsunami size by affecting the deformation of earth surface (Okal, 1988; Kanamori, 1972).

Simplified seismic models in terms of fault size, rigidity, reference depth, and dip angle are used to compare with the data compiled and analyzed by Lay et al. (2019). Figure 2 illustrates the cross-section of the megathrust and ocean model. The water depth in Model Suite D is 5 km with

an upper plate slope of 2°. Three sets of faults are considered. The first set utilizes the fault width determined from the scaling relation of Allen and Hayes (2017) and the typical 40 GPa rigidity to provide a baseline for comparison. The second set uses a narrow fault with half of the width from Allen and Hayes (2017) and 40 GPa rigidity to mimic the common situation that the majority of slip concentrates on the part of the fault area. The third set uses a narrow fault and by changing the rigidity explores the effect of source region rigidity on tsunami size.

Figure 27 shows the results from the wide fault with 40 GPa rigidity at 0, 5, 10, 15, and 20 km reference depth. The results in section 3.2 show the tsunami amplitude increases with the dip angles. The max sea surface elevations are thus computed for 5° to 25° dip angles and plotted as ranges. A value of 40 GPa is approximately the average rigidity of great earthquakes with a source depth from 15 to 35 km (Lay et al., 2012). The tsunami amplitude appears to saturate between 10 to 15 km reference depth. The wider and deeper fault, especially with a small dip angle, can extend below dry land truncating the energy contributing to the tsunami. The lower edge of the green band in the Figure 27, which corresponds to 0 km reference depth, shows a prominent drop from Mw 8.0 to 8.5. This can be explained by Figure 28, which shows the fault produces subsidence at the shoreline with little contribution to the tsunami. When the Mw is 9.0, the reference depth is 0 km, and the dip angle is 5°, the corresponding maximum surge is abnormally small for the magnitude because the entire subsidence is on land. The cases with a 20 km reference depth cover the observed tsunami with amplitude less than 1 m. This points to the concept that small tsunamis may be generated by earthquakes with high rigidity at the deeper part of the plate interface. Models with 0-15 km reference depth cannot cover the major events, indicating that 40 GPa rigidity is not typical for shallow-slip earthquakes. It is infrequent for an earthquake with a deep fault to have large magnitude, so the bands of results for 15 and 20 km reference depths are truncated at Mw 8.5 and 8.0, respectively.

Reducing the fault size can increase the slip and shift the initial tsunami wave to deeper water for a given Mw. Larger slip corresponds to larger seafloor deformation and initial waves at deeper

water give a larger shoaling coefficient that increases the surge at the shore. With the narrow fault, the models can cover tsunami events up to ~5 m observed amplitude, including those generated by earthquakes without shallow rupture, but could not cover all of the smaller tsunamis, especially whose amplitude is lower than ~0.4 m (Figure 29). This suggests that seismic faults that produced the small tsunamis are deeper and larger in area. However, this does not rule out some of the recorded tsunami wave amplitudes being smaller than the actual values due to limited measurements available at tidal gauges. Regardless of whether it is a narrow fault or a wide fault, the bands with a reference depth of 20 km are wider than the others. This is because the lower bound corresponds to 5° dip angle and the majority of the deformation is on the land. A rigidity of 40 GPa is an overestimate for the shallow-slip earthquakes 0 to 15 km depth, where the rigidity can range from 5 to 30 GPa (Lay et al., 2012; Bilek & Lay, 1999).

Reducing the rigidity is more effective to increase slip for a given earthquake magnitude than halving the fault width, which only doubles the slip. By decreasing the rigidity from 40 to 5 GPa, the slip can multiply by a factor of 8, which produces a much larger tsunami. For cases with rigidity less than 40 GPa, the rigidity of the fault below 15 km from the sea surface is 40 GPa, since low rigidity is not applicable for large depth. Earthquakes with 10 GPa rigidity can explain many of the shallow-slip events. Figure 30 shows that models with 5 GPa rigidity can cover most tsunami earthquakes, except for 1998 Papua New Guinea earthquake, in which a submarine slump also played a role in the tsunami amplitude (Synolakis et al., 2002), and 2006 Java earthquake, which may have focused the run-up on Central Java due to a submarine canyon ( Fritz et al., 2007). Massive coastal slumping also contributes to the 1992 Flore tsunami as well (Hidayat et al., 1995). The model results also provide a reasonable description of the largest events from the records. The 2004 Sumatra event likely has a peak tsunami augmented by a splay fault, which becomes steeper as it approaching the seafloor (Moore et al., 2007), whereas, the Tohoku 2011 earthquake has a dip angle at ~10° (Shao et al., 2011).

Figure 31 provides selected results from Figures 27, 29, and 30 to best cover the full range of the observed data and illustrate how the tsunami size depends on earthquake moment magnitude as well as rigidity, reference depth, and fault size. Models with typical rigidity of 40 GPa and standard fault size from Allen and Hayes (2017) can only account for small tsunami events generated by earthquakes with no shallow slip. Besides narrowing down the fault, decreasing the rigidity, especially for shallow earthquakes, can increase the slip and extend the coverage to large tsunami events with surface elevation reaching ~45 m. For earthquakes with a certain Mw, although changing the depth of the source can change the shape of the seafloor deformation to affect the tsunami size, the depth-dependent rigidity directly affects the slip, and plays a primary role in determining the tsunami size. The low rigidity at shallow depths confirms the mechanism of tsunami earthquakes and explains the large range of observed sea surface elevations for earthquakes of a given magnitude.

# Chapter 4

## Conclusions and Recommendations

A parametric study with simplified seismic and bathymetry models can systematically describe the relationship between peak tsunami amplitude and key seismic parameters. Implementation of seismic models beneath a flat seafloor provides a quantitative relationship between tsunami size and seafloor deformation in terms of dip angle and fault depth. The results show vertical attenuation and horizontal spreading of seafloor excitation over the water column and large uplift over a small area does not necessarily translate to high tsunamigenic potential. The use of an abutting 2° upper plate slope explains the relative spatial position between the fault and shoreline as the dip angle and reference depth vary. Wave shoaling and the percentage of wave energy that propagates to the shore are affected by the water depth where the earthquake occurs. The subsidence also contributes to the surge, and the wave amplitude at the shore is also influenced by the fault width, and water depth. By comparing the computed and recorded maximum sea surface elevations, it is confirmed that the rigidity plays a leading role in the size of a tsunami for a given Mw. The results quantitatively support that the disproportionate flood hazards from tsunami earthquakes are due to the low source region rigidity at the shallow depth. Other geophysical factors also interact with each other and jointly determine the size of the tsunami at the secondary level.

Many mature technologies have been successfully applied in warning of far-field tsunamis. The Global Seismographic Network as well as other seismic observation networks, like the Advanced National Seismic System and volunteering monitoring, transmit waveform data in real-time for rapid earthquake assessment. Automatic and rapid post-processing of seismic wave data allows tsunami warnings to be issued within 30 minutes after an earthquake. DARTs can capture the tsunami waveforms and help improve the reliability of tsunami warning, and this is very important when the rupture is slow. However, for local tsunami events, recorded water-level data

is often lacking until the waves hit the shore. A large-scale dense cabled seafloor observation network called the S-net, which has been installed along the Japan Trench since May 2016, provides real-time tsunami data by using ocean bottom pressure sensors (Mochizuki et al., 2018; Inoue et al., 2019). The S-net successfully detected the 2016 Fukushima tsunami with Mw 7.4 (Gusman et al., 2017). For regions lacking a real-time tsunami observation system, it is very important to improve the rapid tsunami forecast by detecting long-period signals in real-time seismic data (Lay et al., 2019). Since the rigidity decreases updip, the focal depth estimated immediately after an earthquake might shed light on the potential of a tsunami earthquake. There two orders of magnitude variability in tsunami size for a given earthquake magnitude highlights the importance of pre-determination of source region rigidity in regional tsunami forecast.

This thesis has provided an introduction to the relationship between peak tsunami amplitude and earthquake magnitude improved by fault depth, dip angle, fault size, and source region rigidity. The use of a simplified rectangular fault might bring uncertainties, but provide a generic model to cover and represent the observed events. The model resolution used in this study can capture wave shoaling from the tsunami source to the shore and reflection from landmass. Increasing the resolution of the near-shore part of the model is needed to give a better description of the run-up for site-specific analysis. Future work includes the application of a finite-fault rupture model to a curved surface and to account for rigidity variation with depth in modeling of specific tsunami earthquakes for insights into the specific mechanisms.

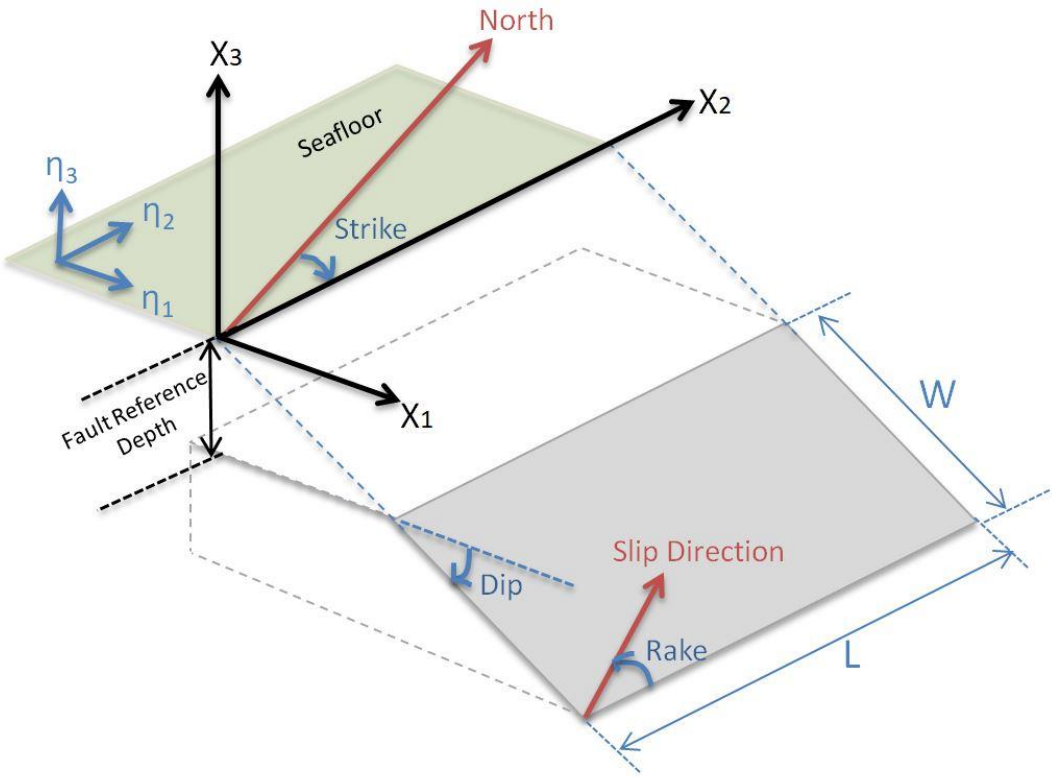


**Figure 1.** Geometry of planar fault model

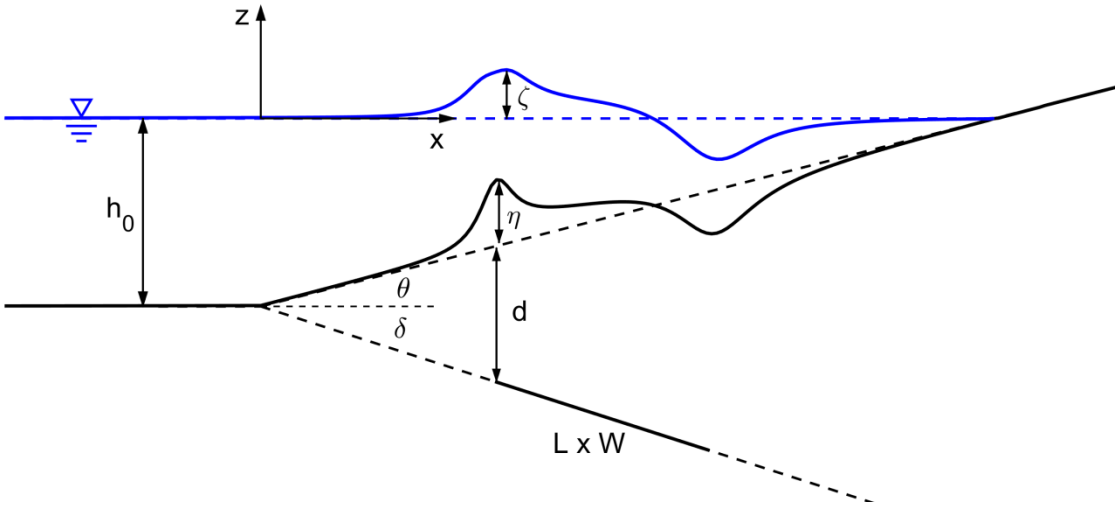


**Figure 2.** Sectional view of setup for NEOWAVE and planar fault model

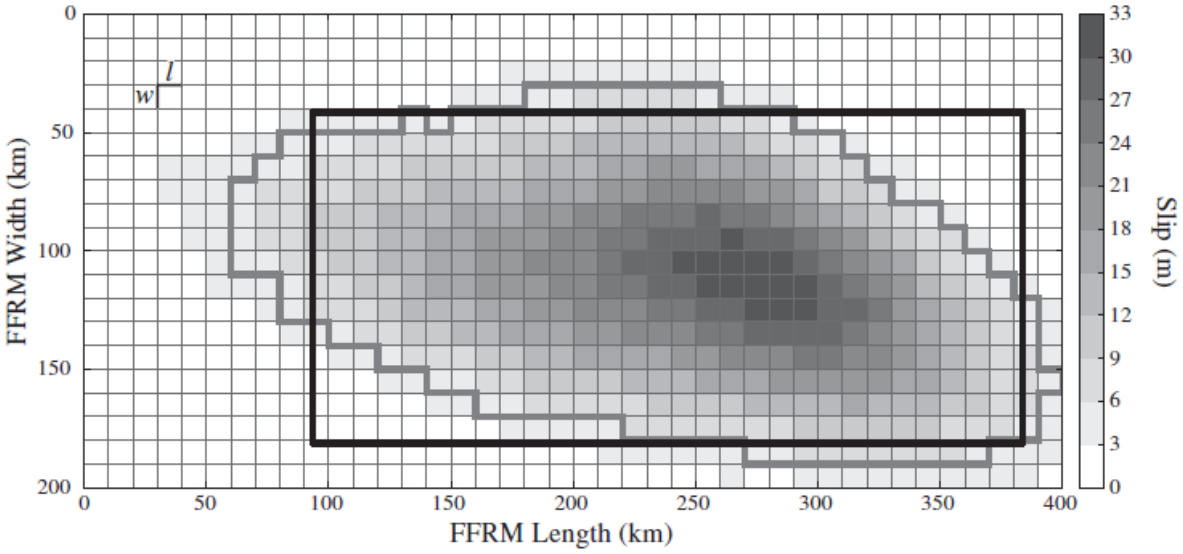


**Figure 3.** Schematic of fault trimming from Allen and Hayes (2017). While trimming the sub-fault that has small slip, the method also introduces area that are not part of the fault.

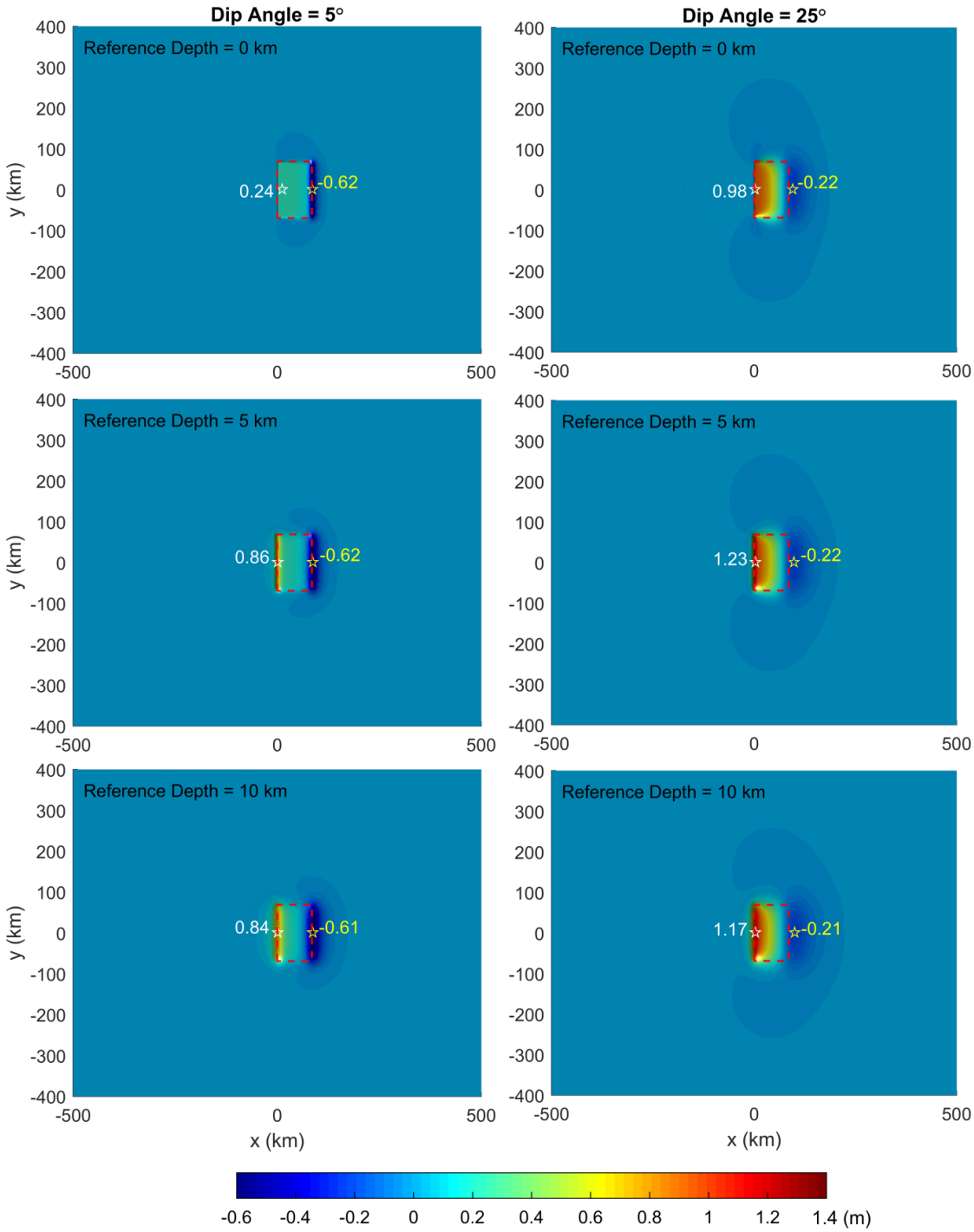


**Figure 4.** Seafloor vertical displacement from Model A as a function of dip angle and reference depth. Red dotted rectangles delineate fault areas. White stars and yellow stars indicate the locations of maximum uplift and subsidence, respectively, and their values are indicated by labels in corresponding colors.

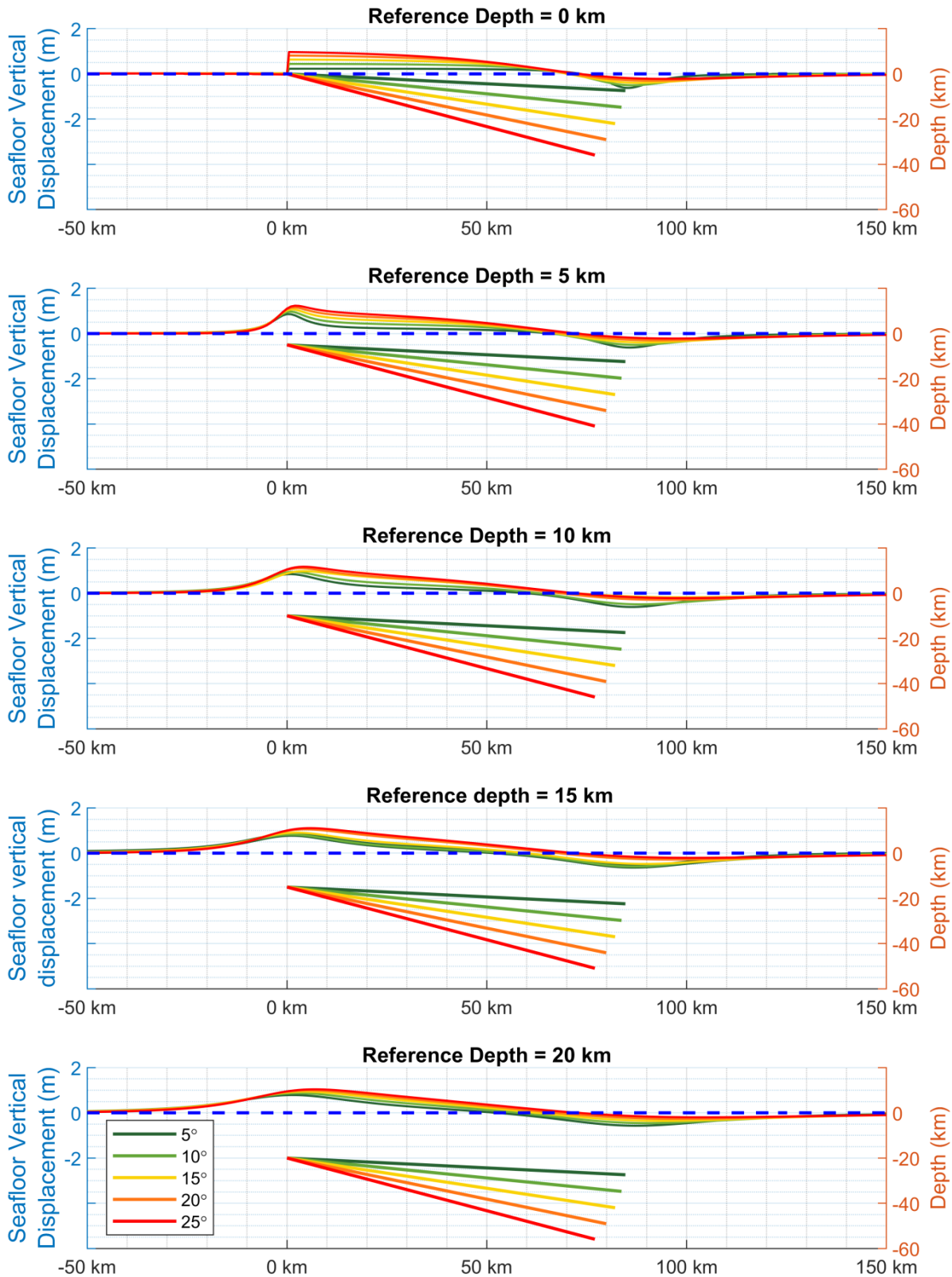


**Figure 5.** Seafloor vertical displacement from Model A along fault centerline as a function of dip angle. The colors indicate the dip angle and the dotted blue line shows the initial seafloor.

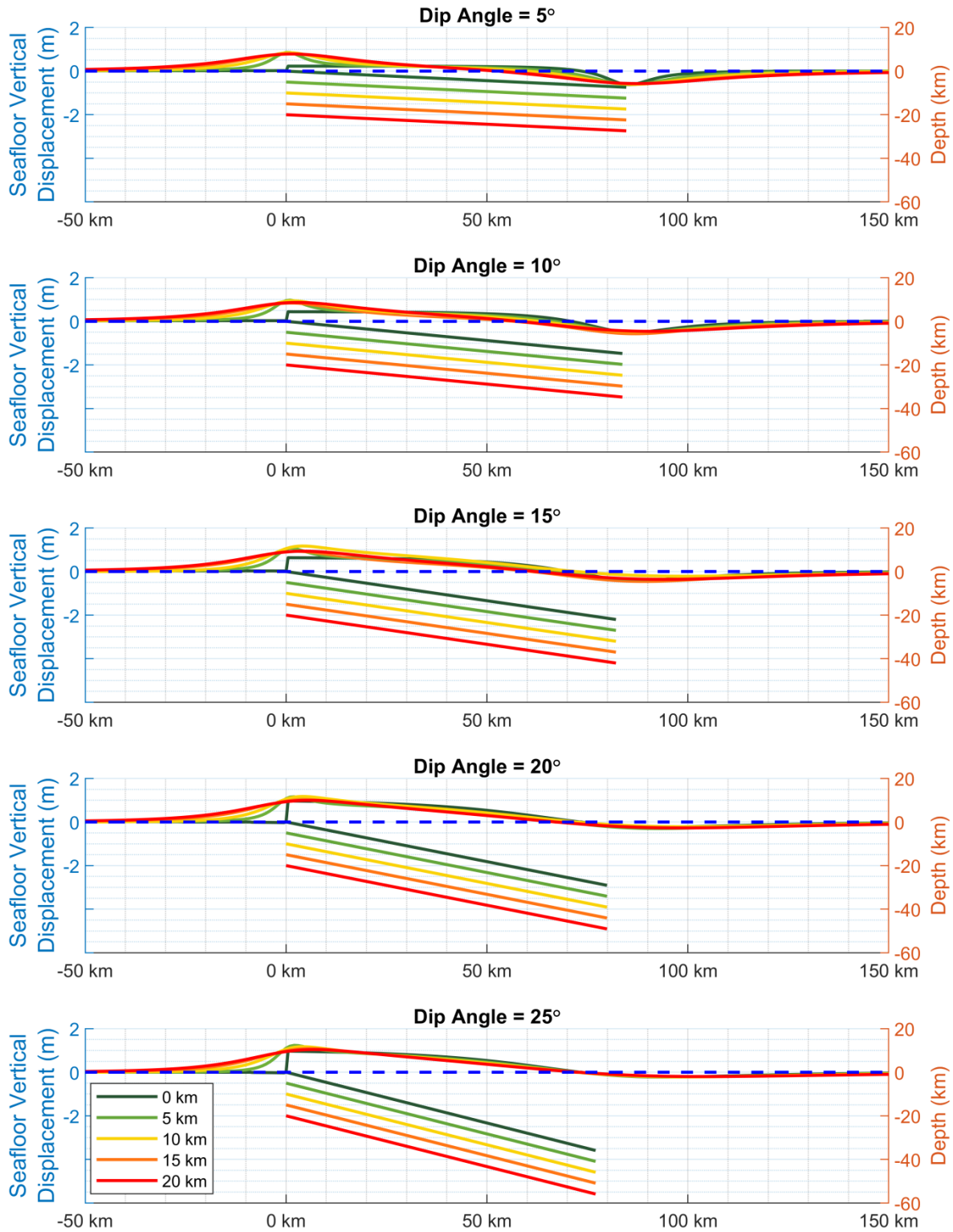


**Figure 6.** Seafloor vertical displacement from Model A along fault centerline as a function of reference depth. The colors indicate the reference depth (at fault upper edge) and dotted blue line shows the initial seafloor.

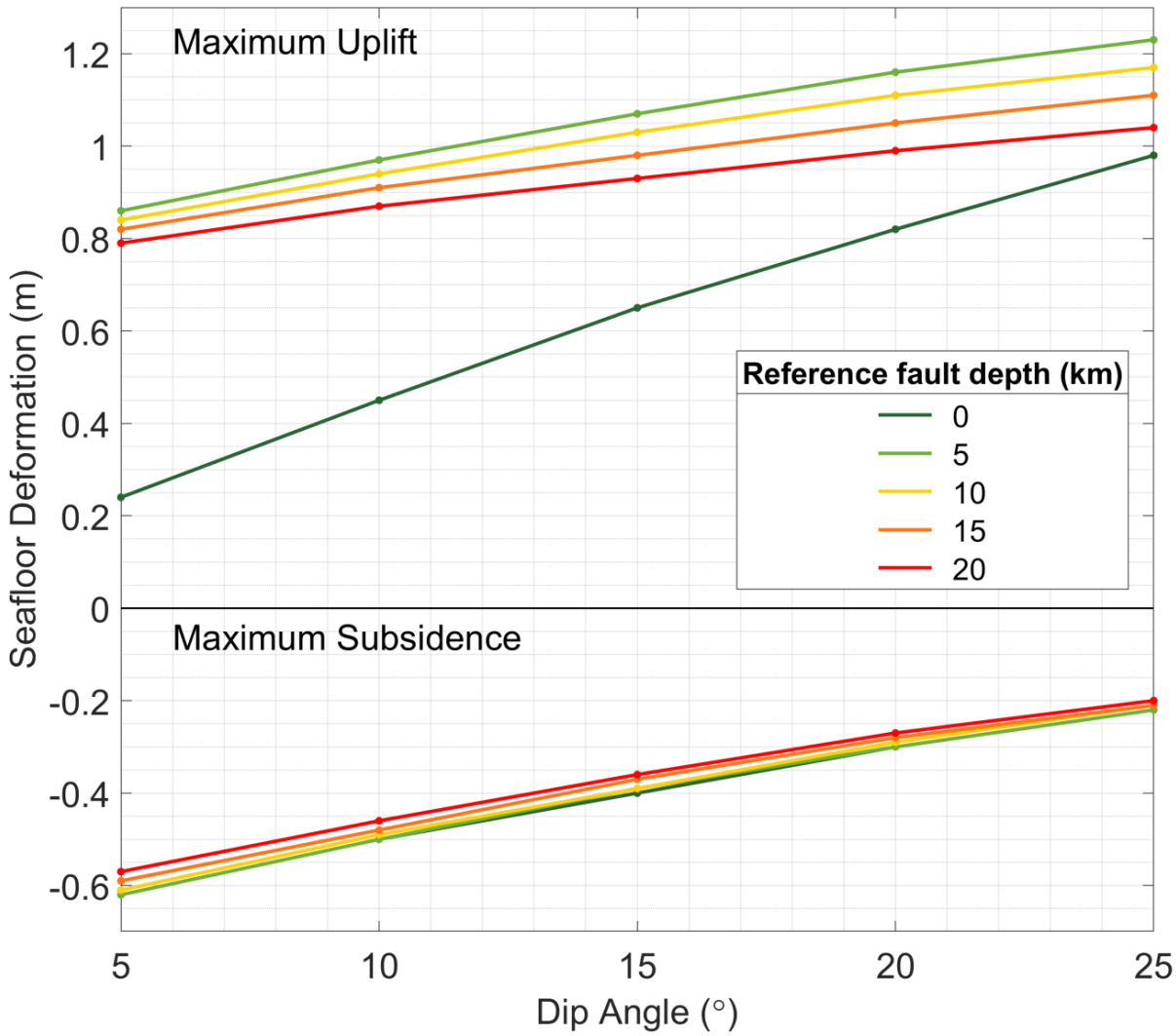


**Figure 7.** Maximum uplift and subsidence from Model A as functions of dip angle and reference depth

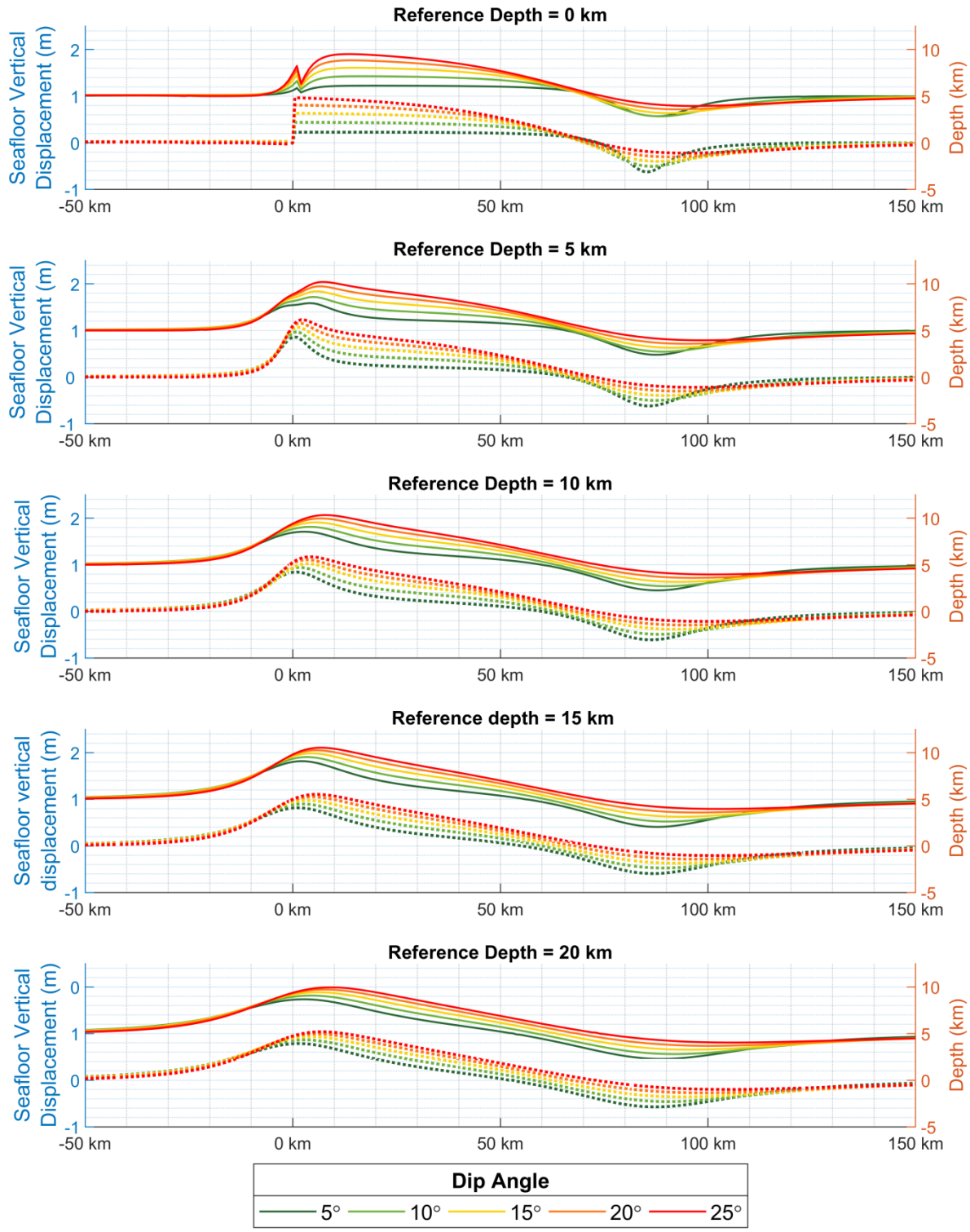


**Figure 8.** Comparison of seafloor deformation and initial sea surface elevation for flat seafloor with 5000 m water depth. Dotted and solid lines denote seafloor vertical displacement and initial sea surface elevations.

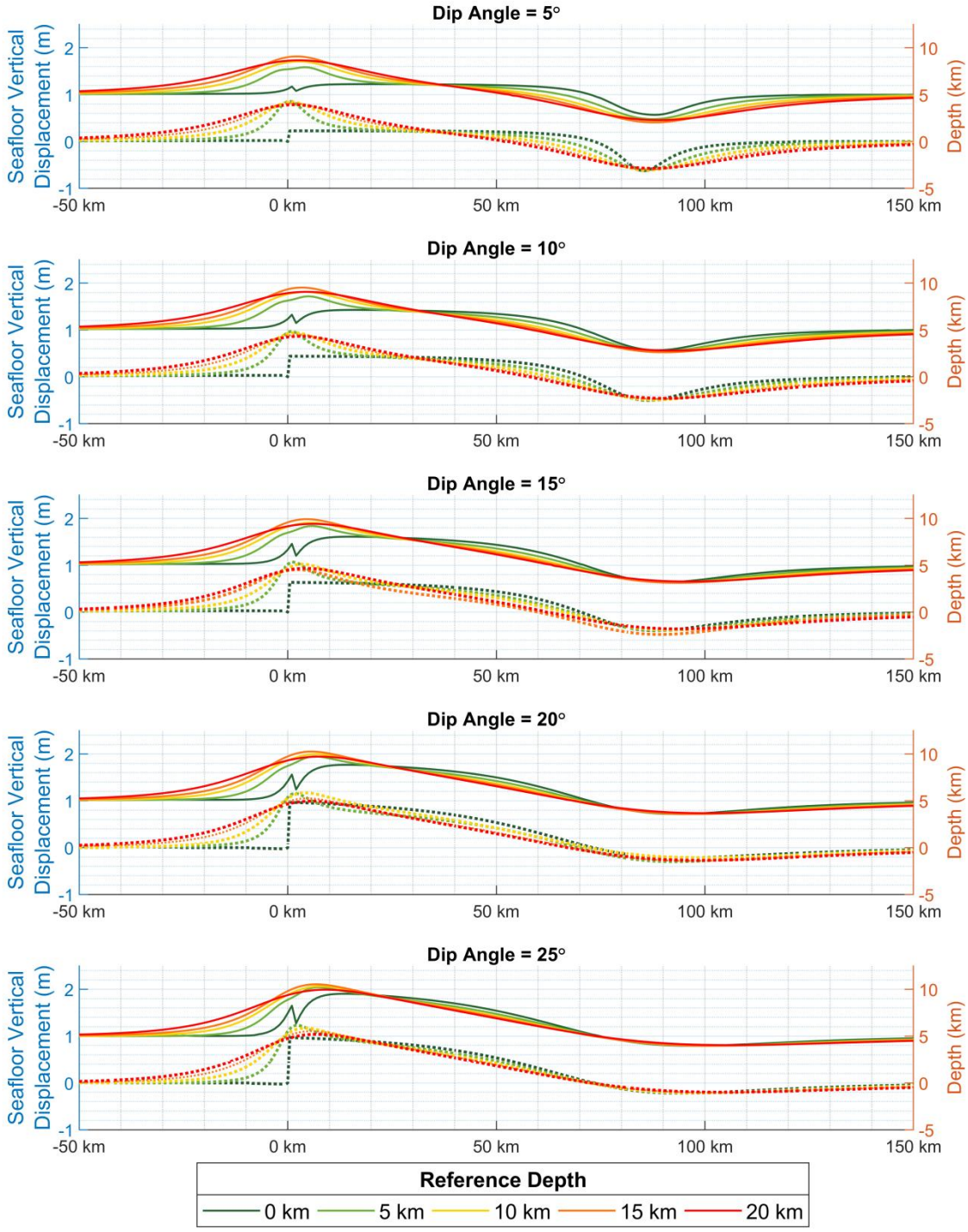


**Figure 9.** Comparison of seafloor deformation and initial sea surface elevation for a flat seafloor with 5000 m water depth. Dotted and solid lines denote seafloor vertical displacement and initial sea surface elevations.

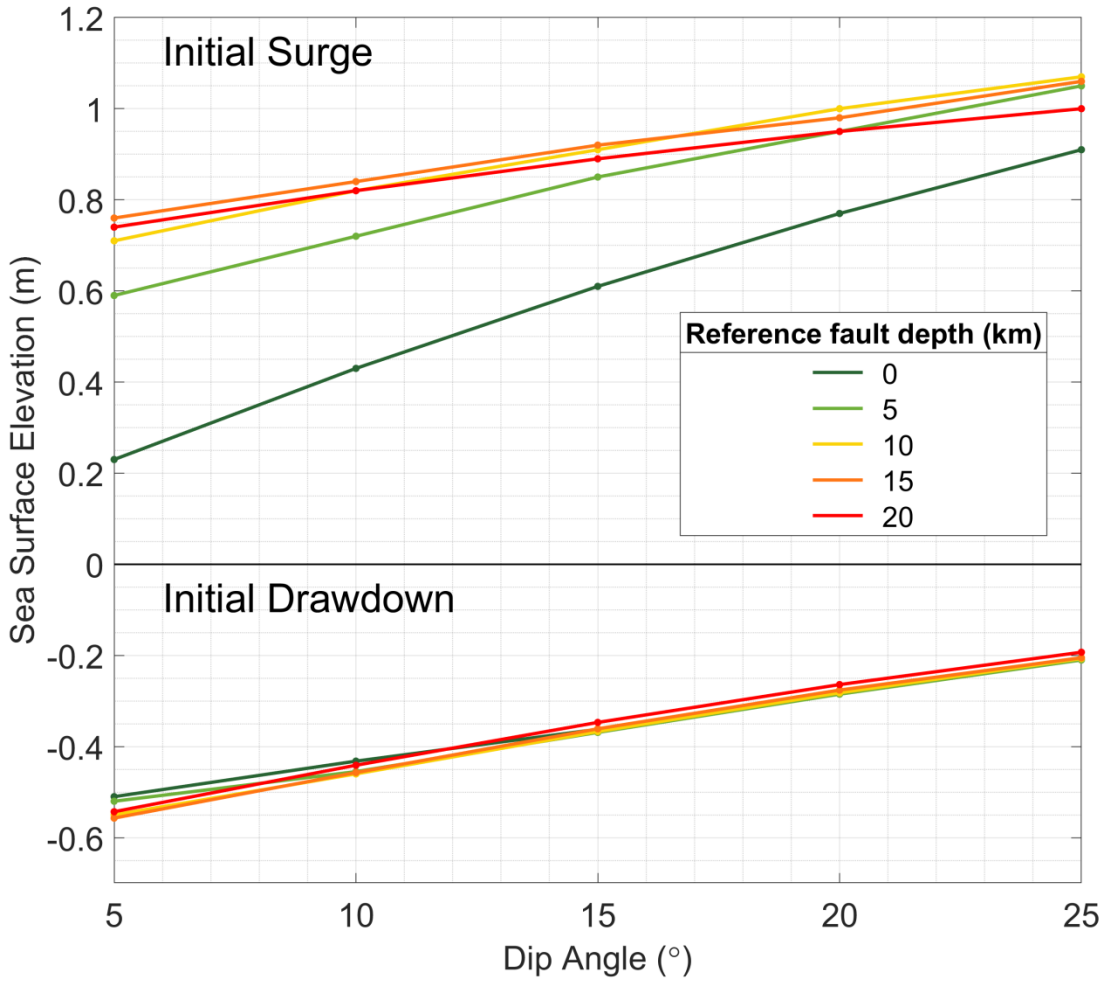


**Figure 10.** Peak surge and drawdown at the end of the rupture for Model A as function of dip angle and reference depth for 5 km water depth.

.

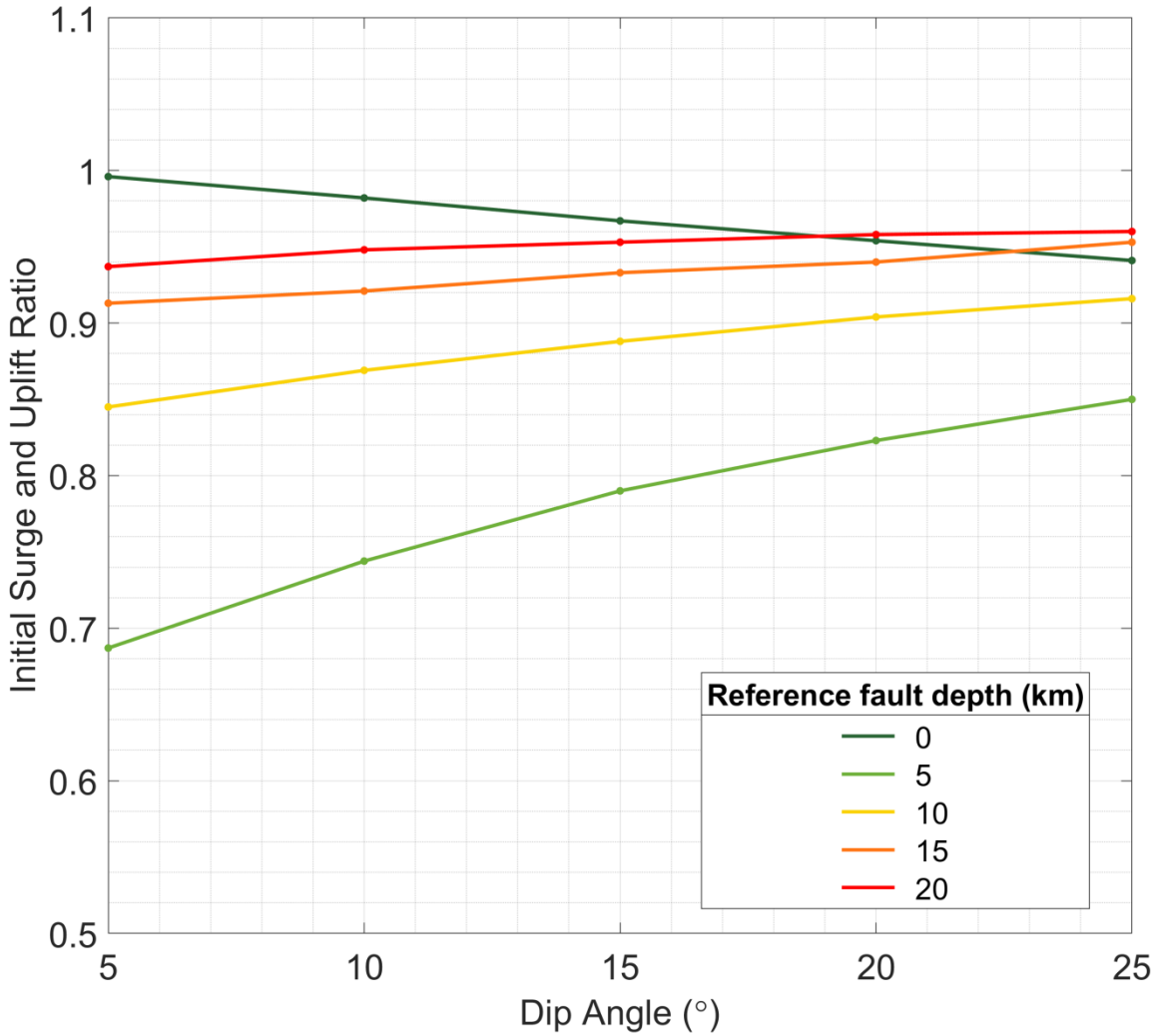


**Figure 11.** The ratio of Initial surge to uplift as a function of dip angle and reference depth.

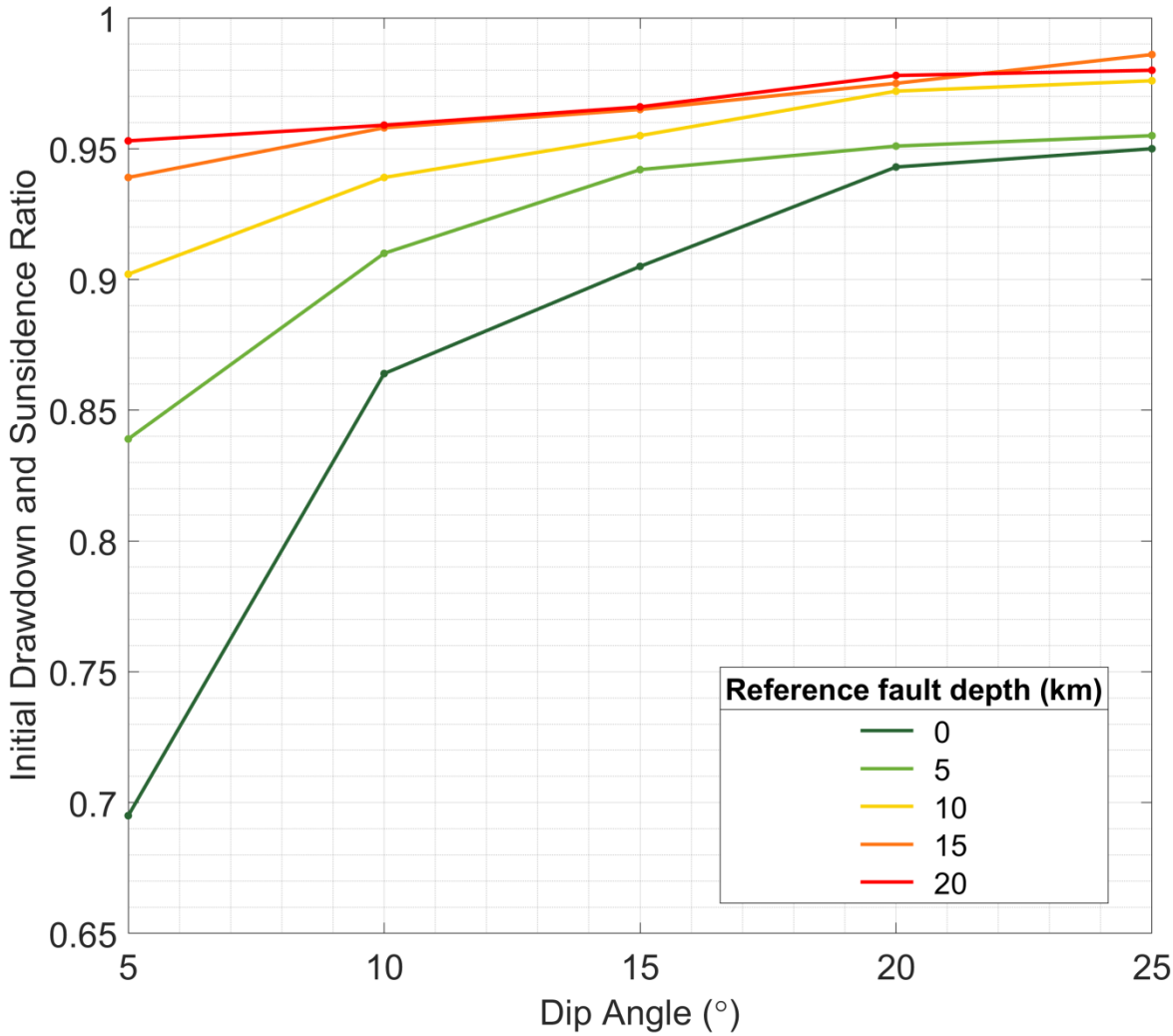


**Figure 12.** The ratio of Initial drawdown to subsidence as a function of dip angle and reference depth.

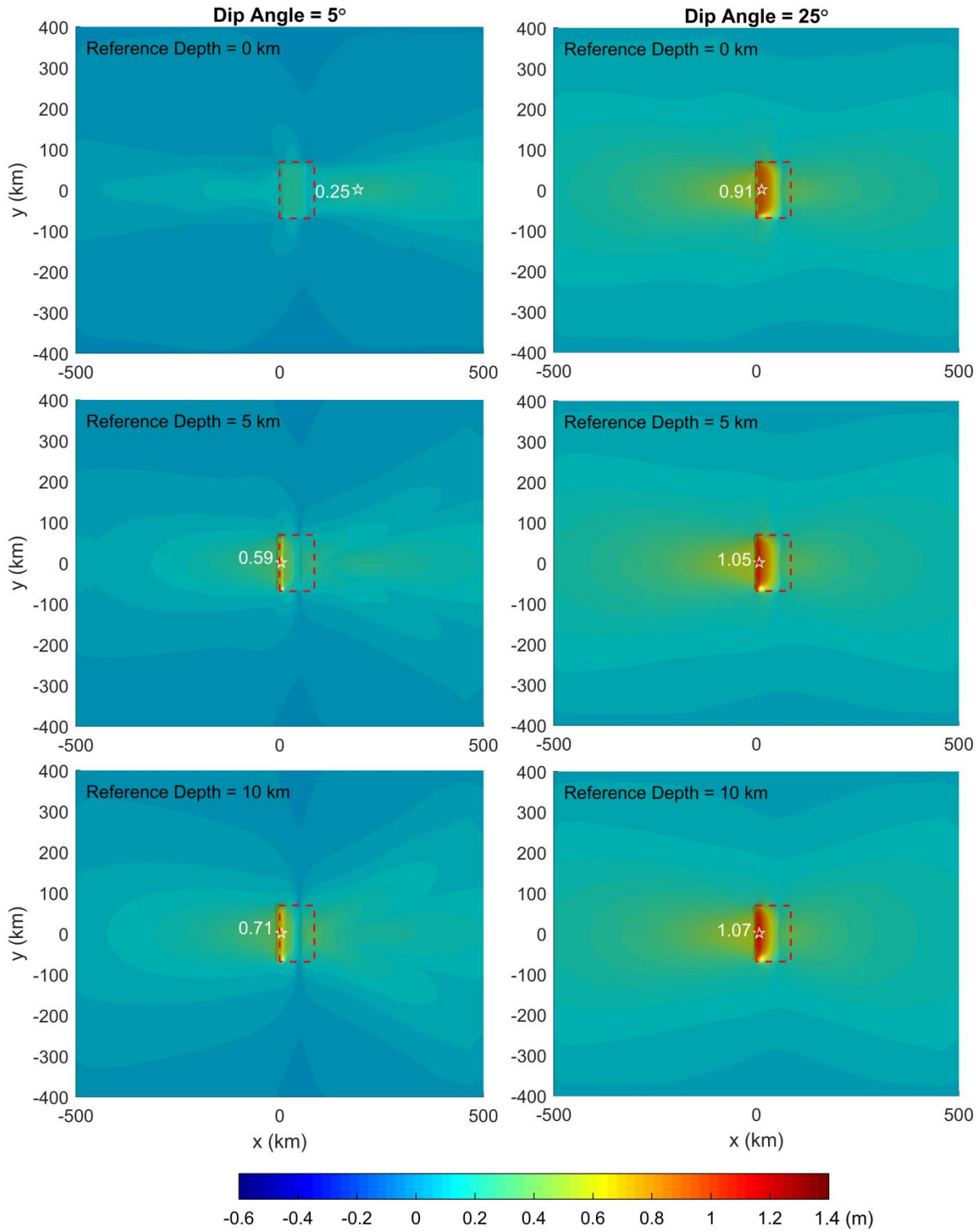


Figure 13. The maximum sea surface elevation from Model A as a function of dip angle and reference depth for 5 km water depth. The red dotted rectangles denote the fault area. White stars and labels indicate the location and maximum sea surface elevation.

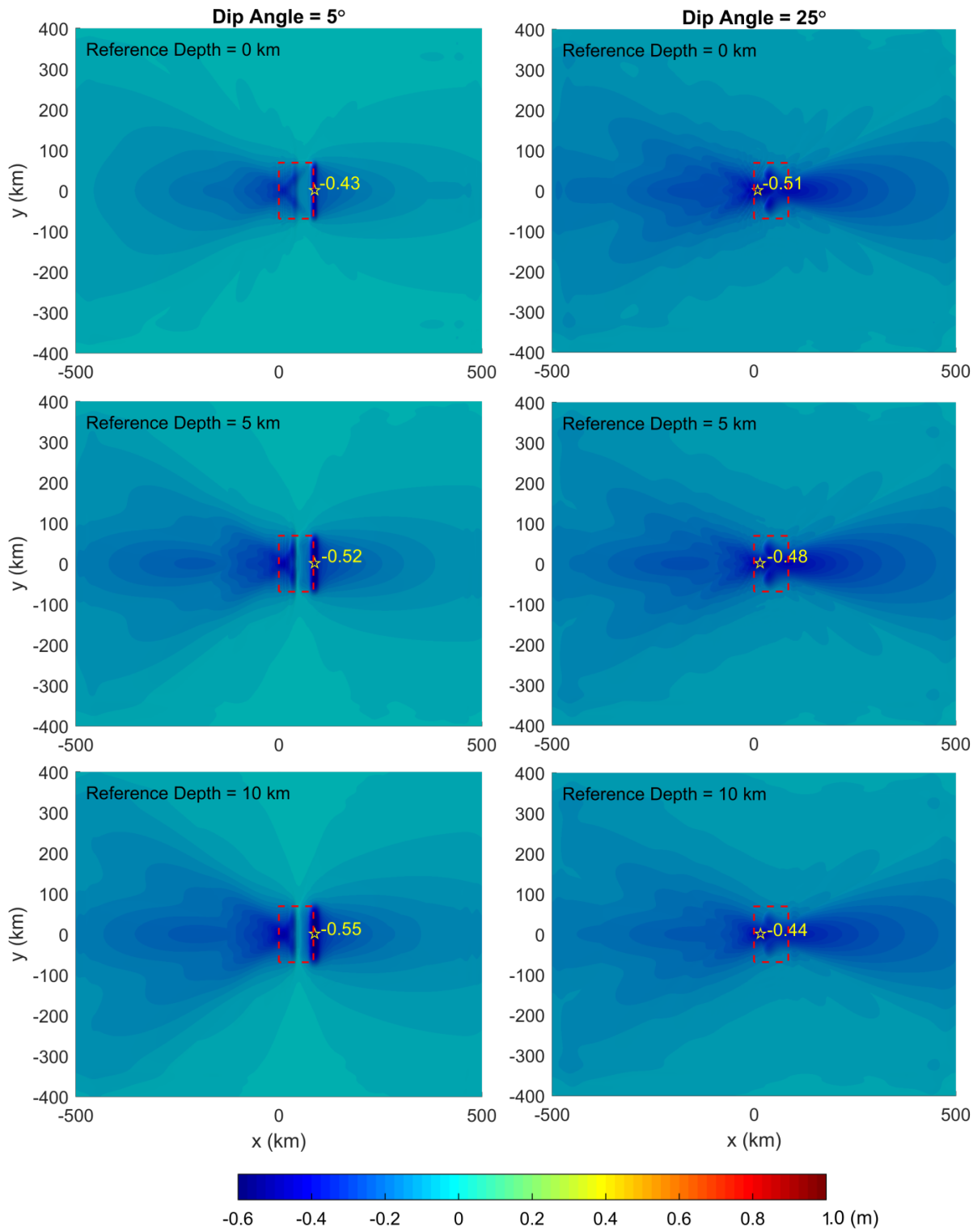


**Figure 14.** The minimum sea surface elevation from Model A as a function of dip angle and reference depth for 5 km water depth. The red dotted rectangles denote the fault area. Yellow stars and labels indicate the location and the minimum elevation.

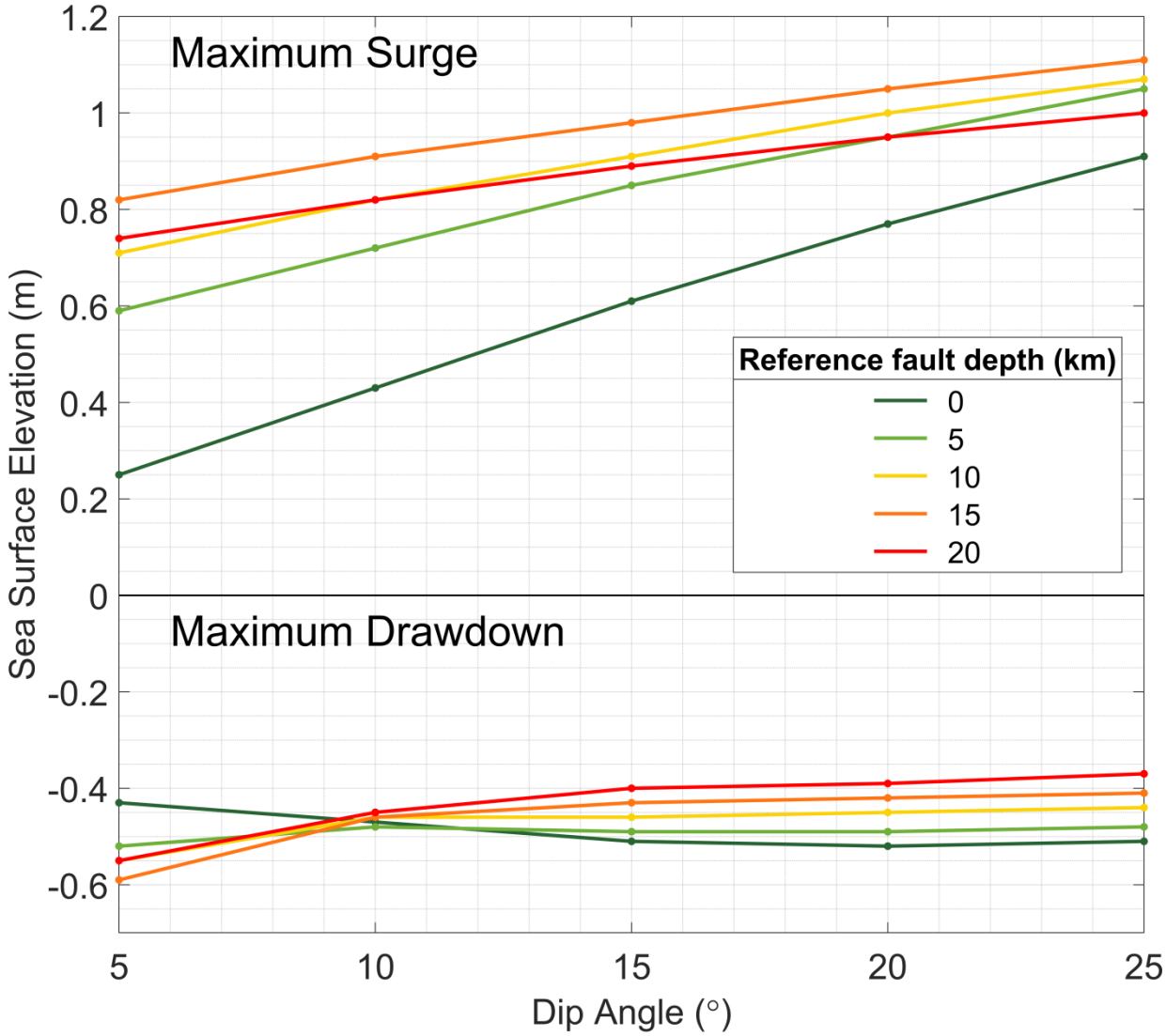


**Figure 15.** Maximum surge and drawdown from Model A as function of dip angle and reference depth for 5 km water depth.

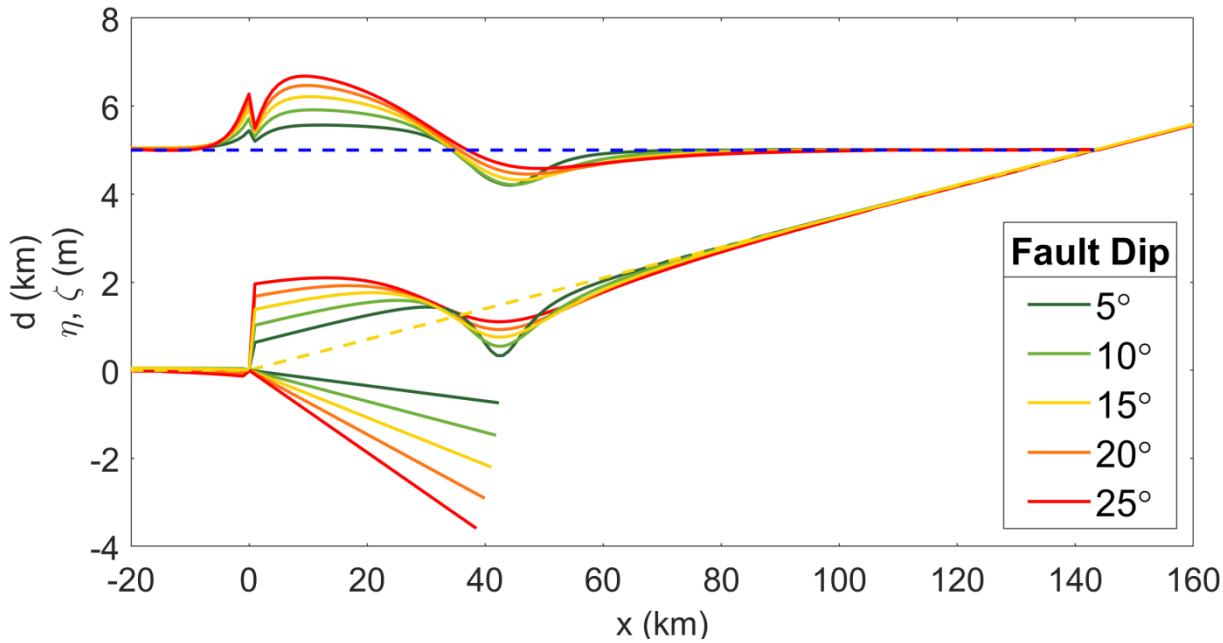


**Figure 16.** Seafloor displacement and sea surface elevation as functions of dip angle for 0 km reference fault depth and 5 km water depth. The dotted yellow and blue lines indicates the initial seafloor with 2° dipping angle and the initial sea surface.

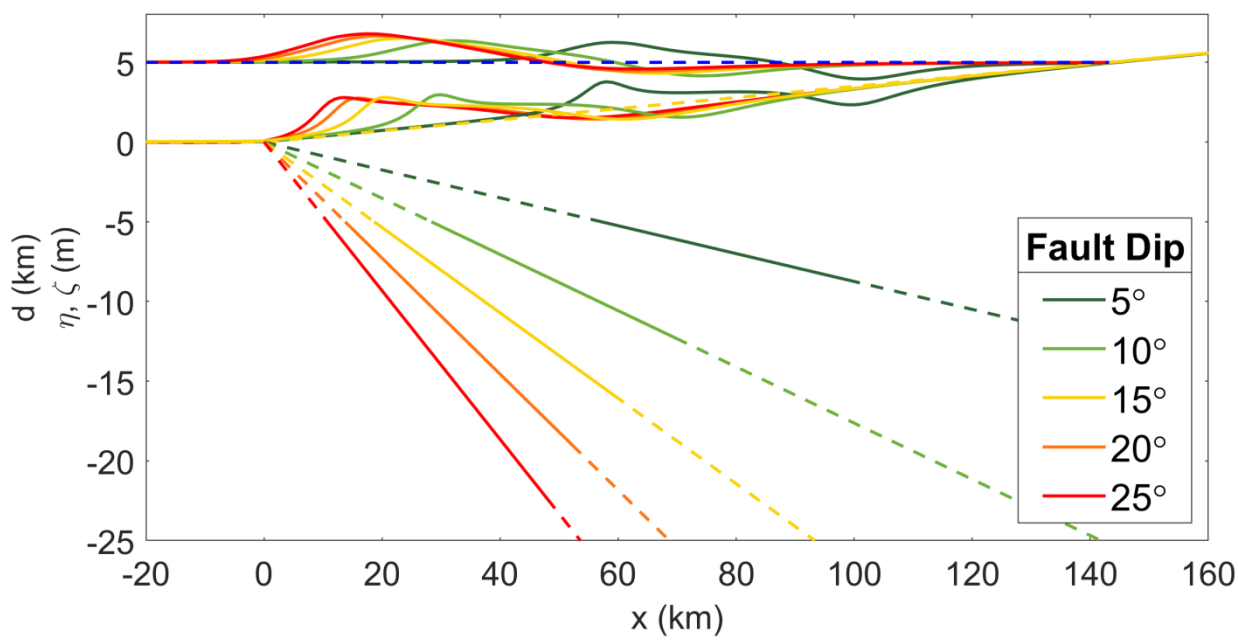


**Figure 17.** Seafloor displacement and sea surface elevation as functions of dip angle for 5 km reference fault depth and 5 km water depth. The dotted yellow and blue lines indicate the initial seafloor with 2° dipping angle and the initial sea surface.

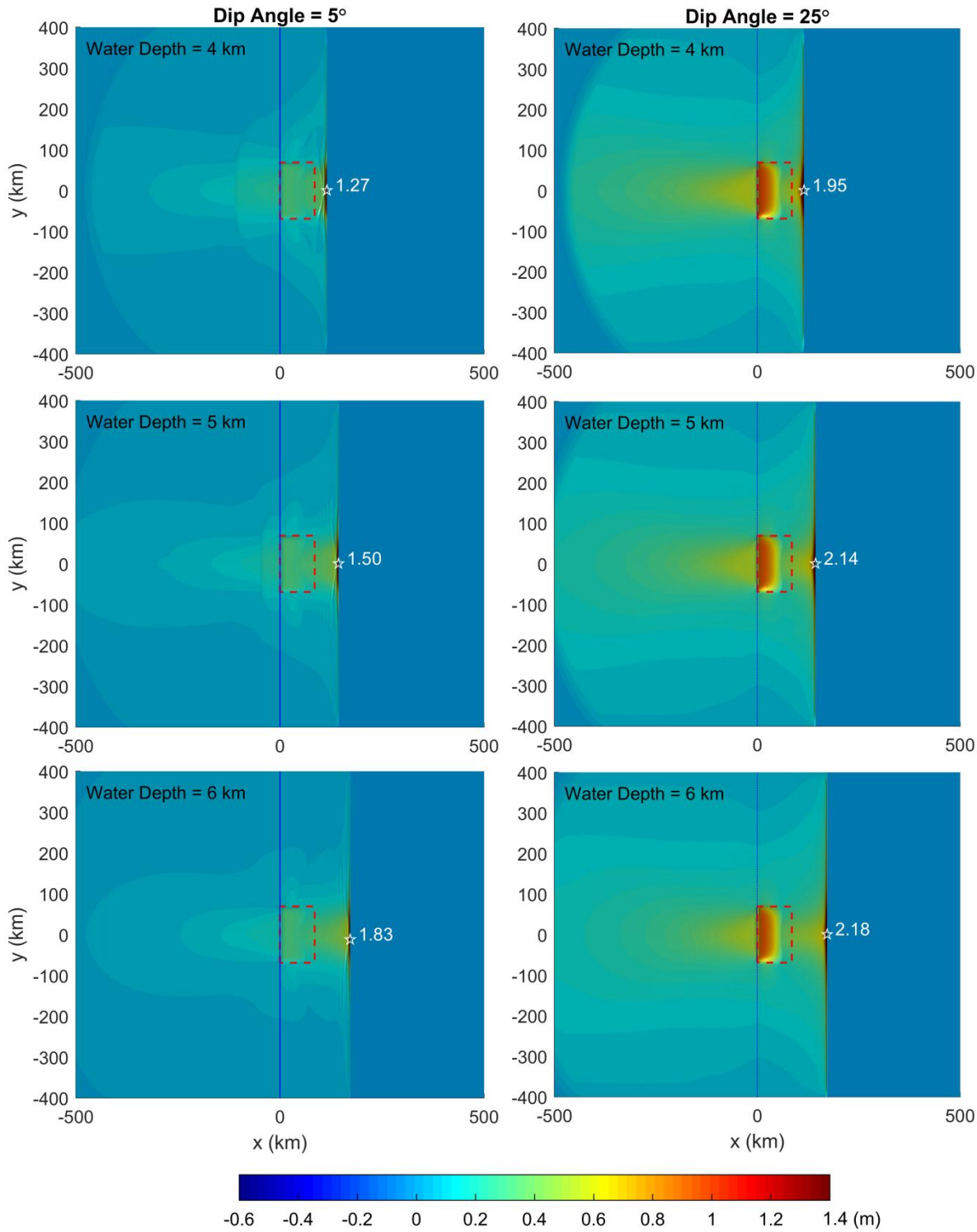


**Figure 18.** Maximum sea surface elevation from Model B as a function of dip angle and water depth for 0 km reference depth. The blue line shows the location of the trench, and the red dotted rectangles denote the fault. The uniformed blue color on the right side of each panel is land. White stars and label indicate the location and the peak surface elevation.

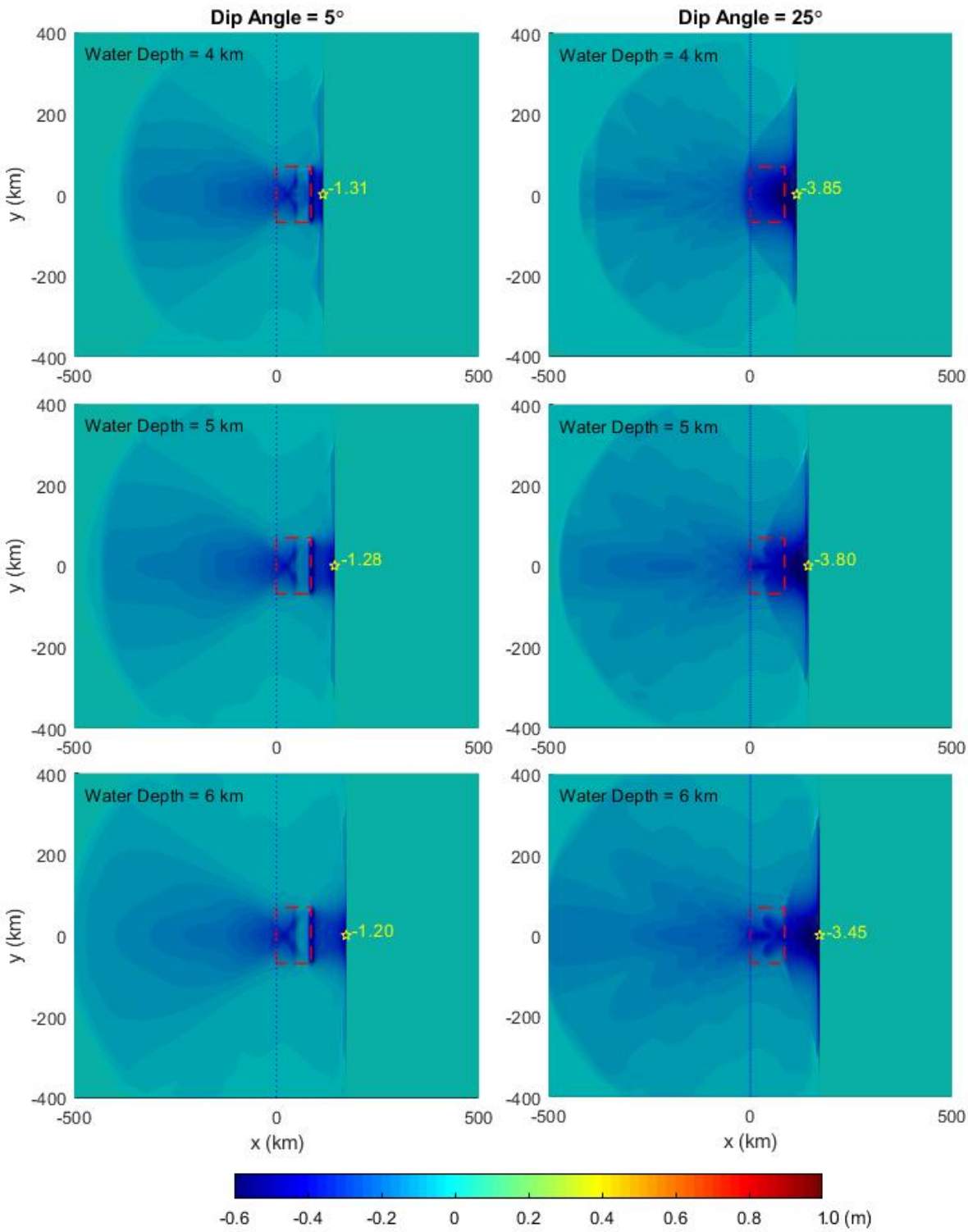


**Figure 19.** Minimum sea surface elevation from Model B as a function of dip angle and water depth for 0 km reference depth. The blue line shows the location of the trench and red dotted rectangles denote the fault area. The uniformed blue color on the right side of each panel is dry land. Yellow stars and labels indicate the location and minimum sea-surface elevation.

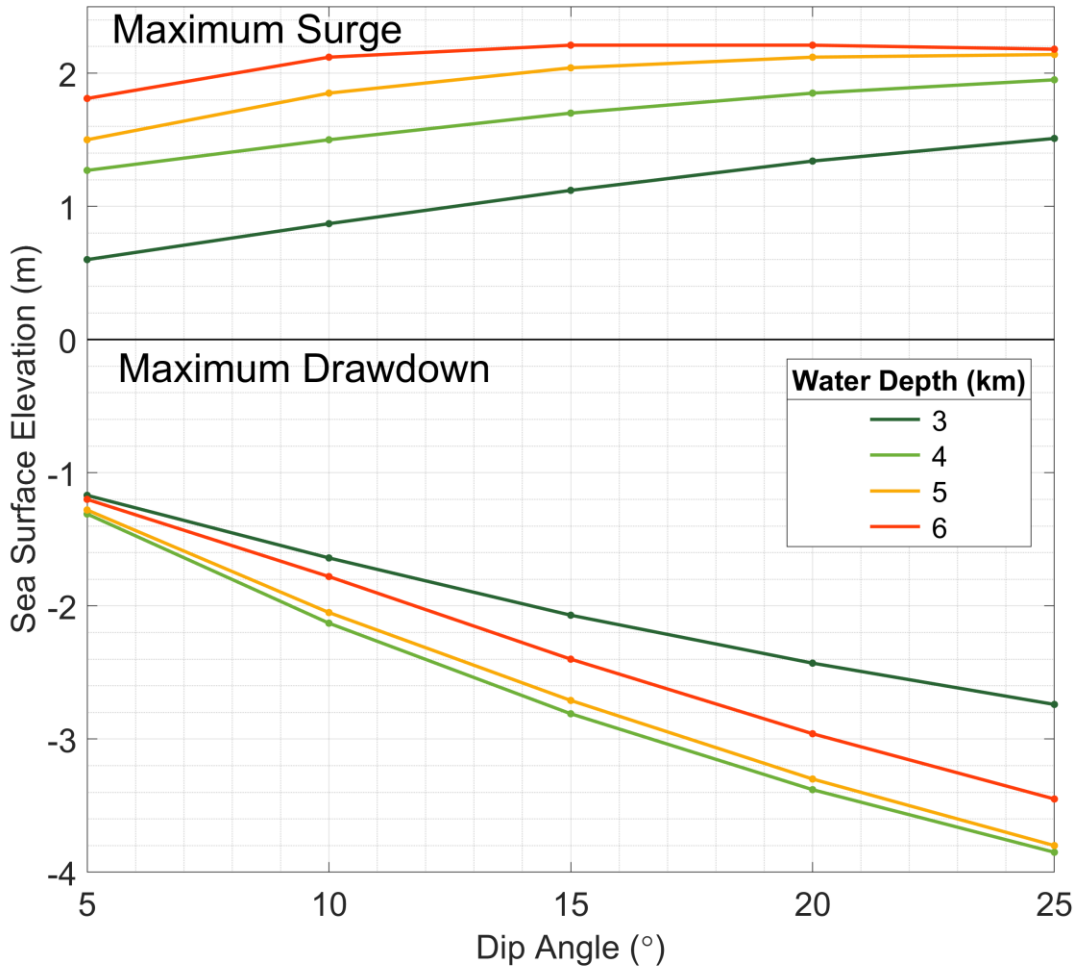


**Figure 20.** Maximum surge and drawdown from Model B as functions of dip angle and water depth for 0 km reference depth.

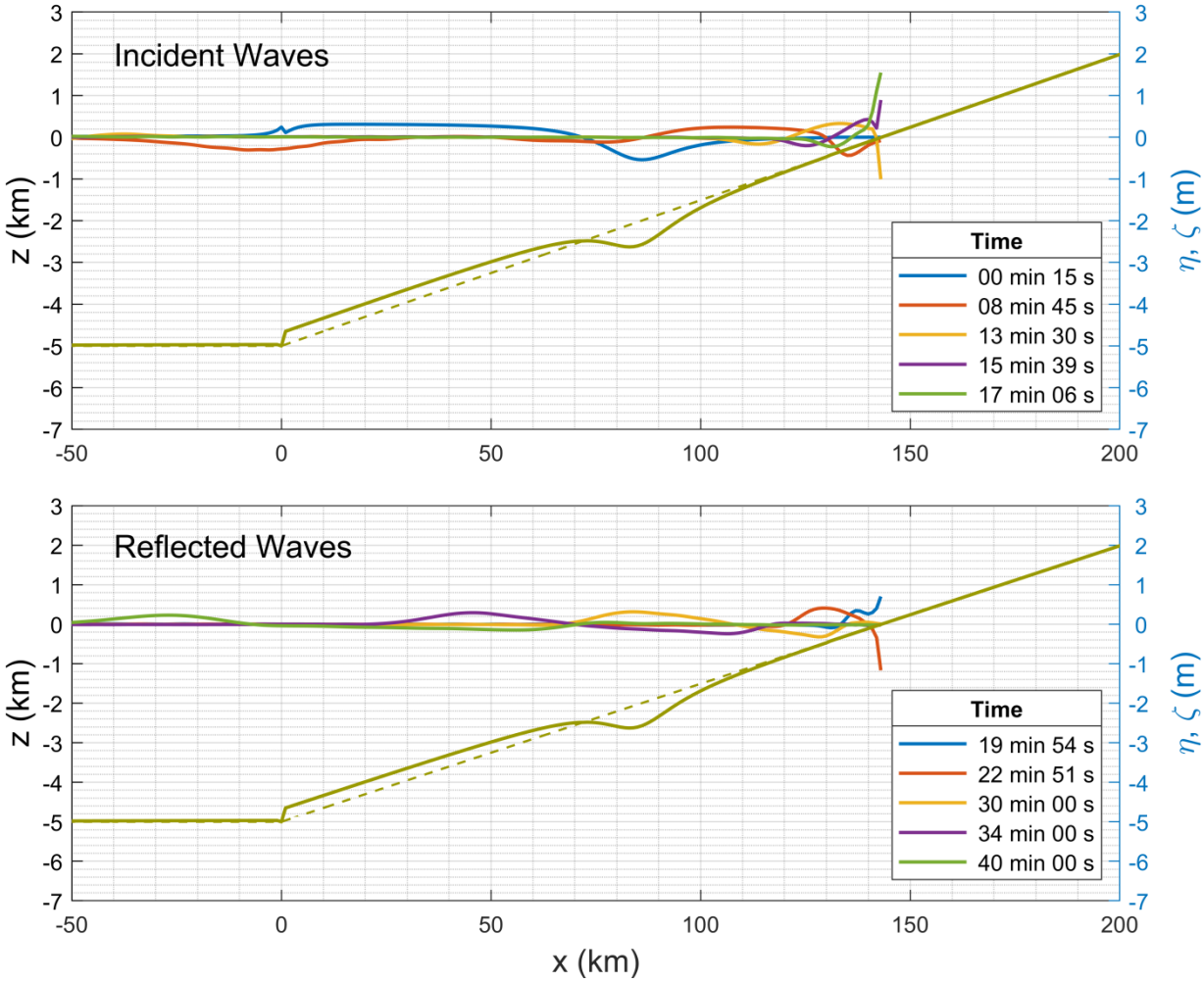


**Figure 21.** Selected wave profiles at different time for 5 km water depth, 0 km reference depth and 5° dip angle. The light brown dashed and solid lines represent the initial and deformed seafloor profiles.

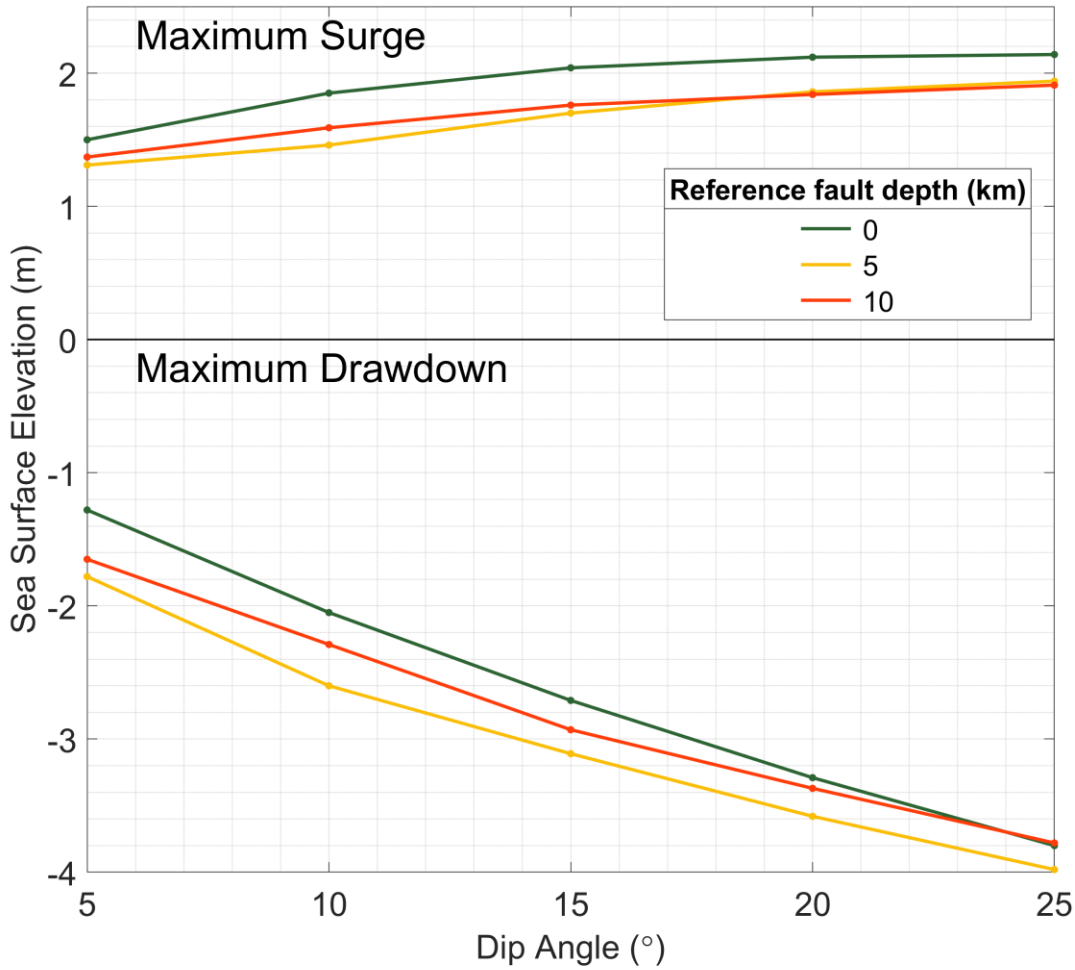


**Figure 22.** Maximum surge and drawdown at shoreline from Model B as functions of dip angle and reference depth for 5 km water depth.

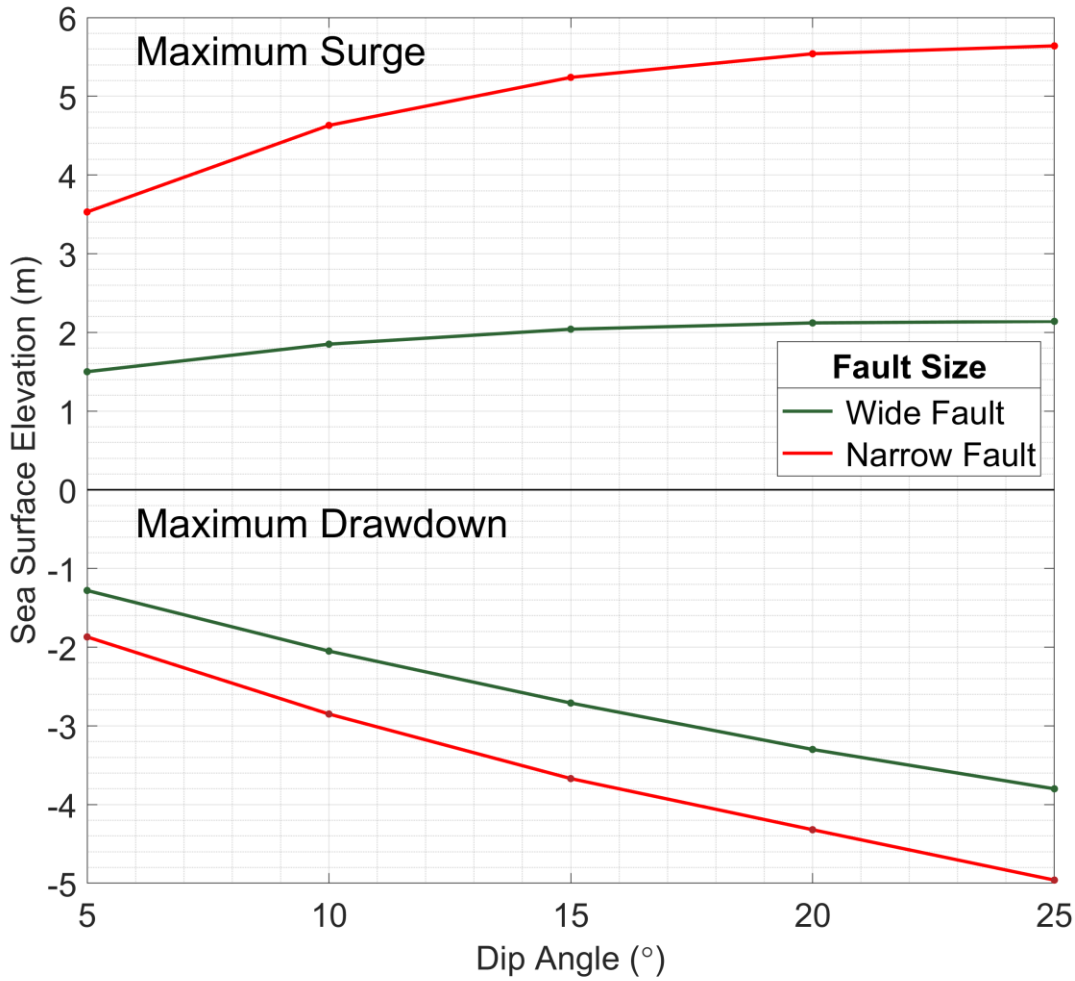


**Figure 23.** Maximum surge and drawdown at shoreline from Model C as functions of dip angle for 5 km water depth and 0 reference depth.

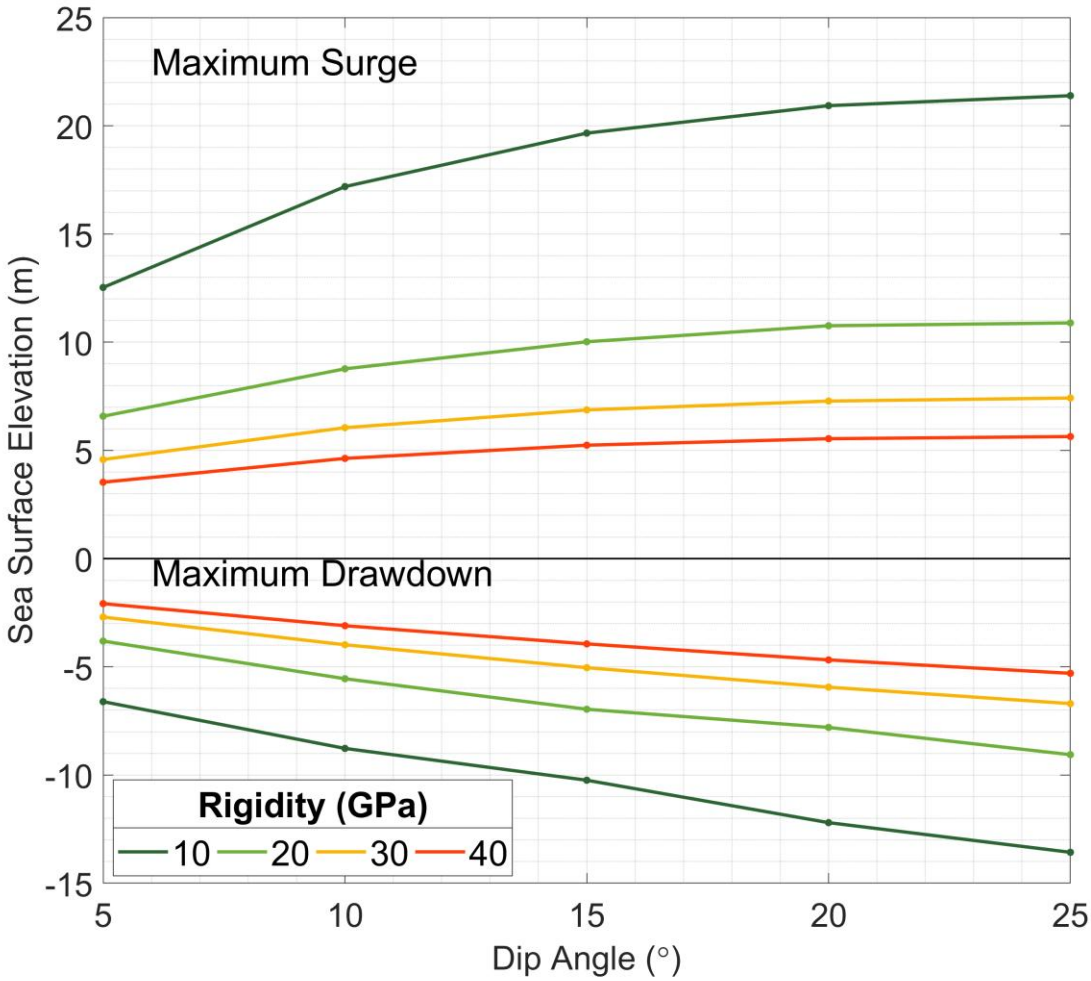


**Figure 24.** Maximum surge and drawdown at shoreline from Model C as functions of dip angle and rigidity for 5 km water depth and 0 reference depth.

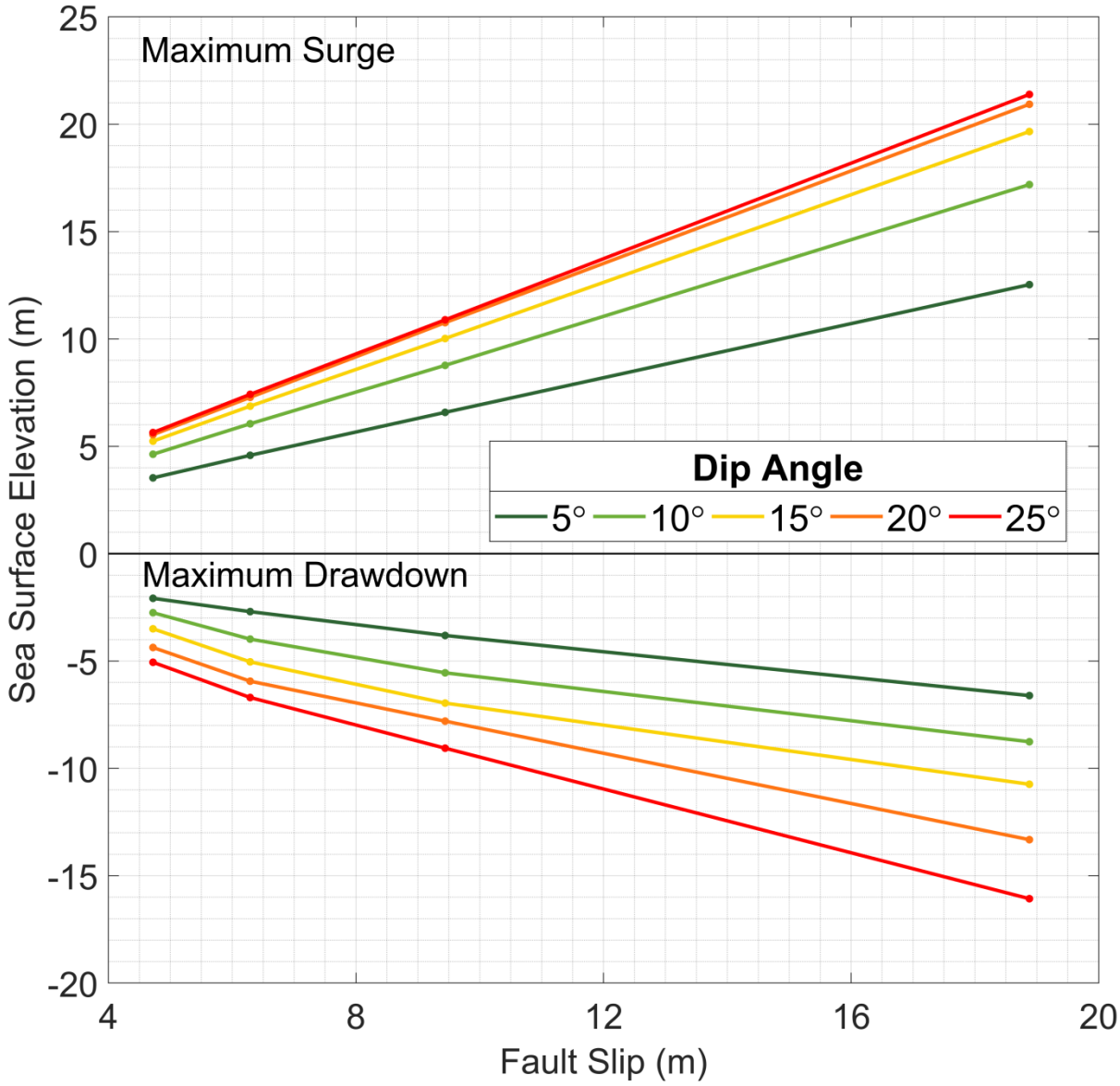


**Figure 25.** Maximum surge and drawdown at shoreline from Model C as functions of dip angle and slip distance for 5 km water depth and 0 reference depth.

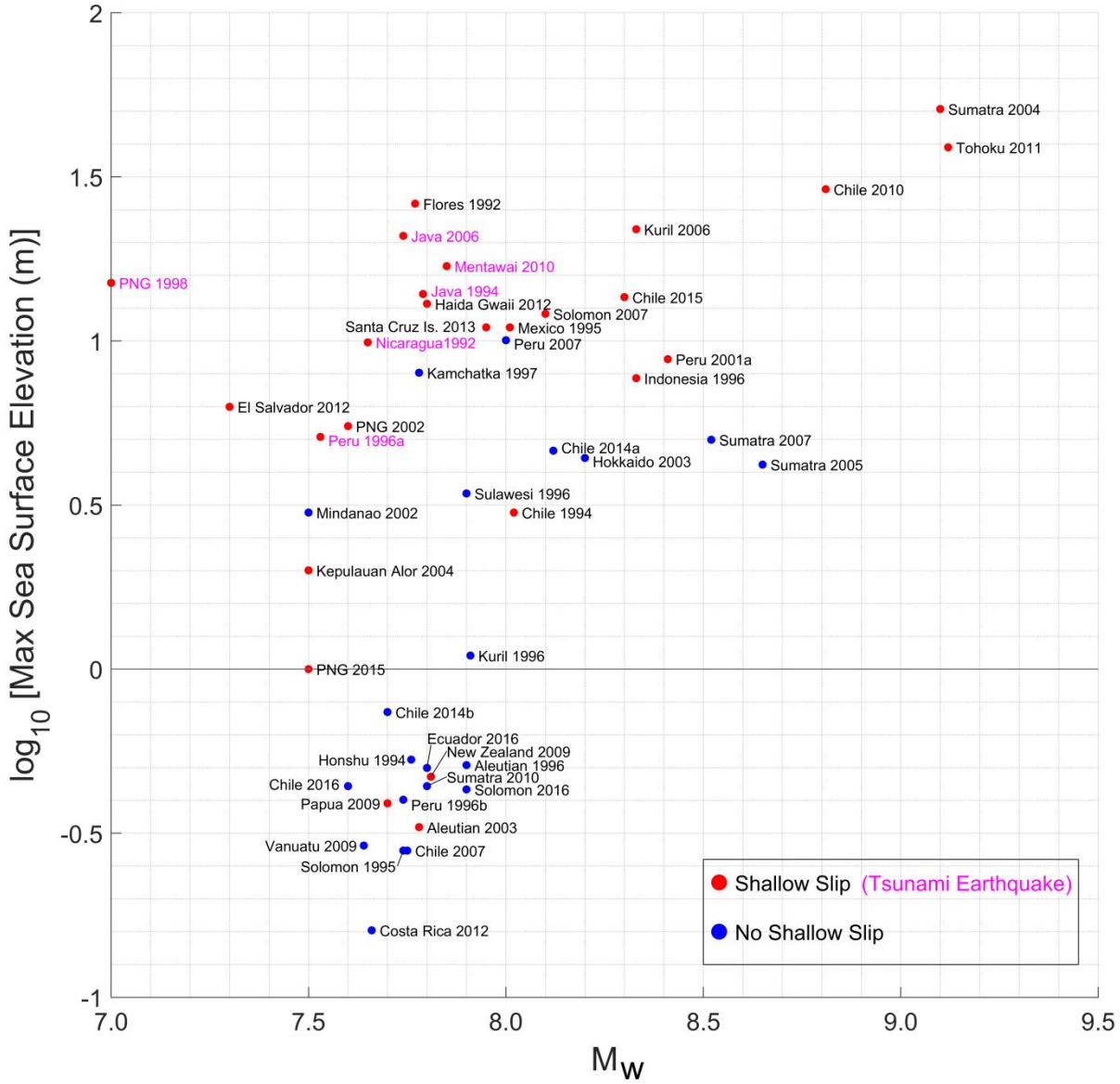


**Figure 26.** $Log_{10}$ of the maximum reported sea surface elevation for 46 large interplate thrust earthquakes from 1990 considered in this study. The maximum surface is defined as maximum run-up from survey after a tsunami or maximum tsunami wave amplitude recorded by the tidal gauge near shore. Each event is estimated whether shallow slip occurred by Lay et al. (2019). Pink colored tsunami names highlight the tsunami earthquake events.

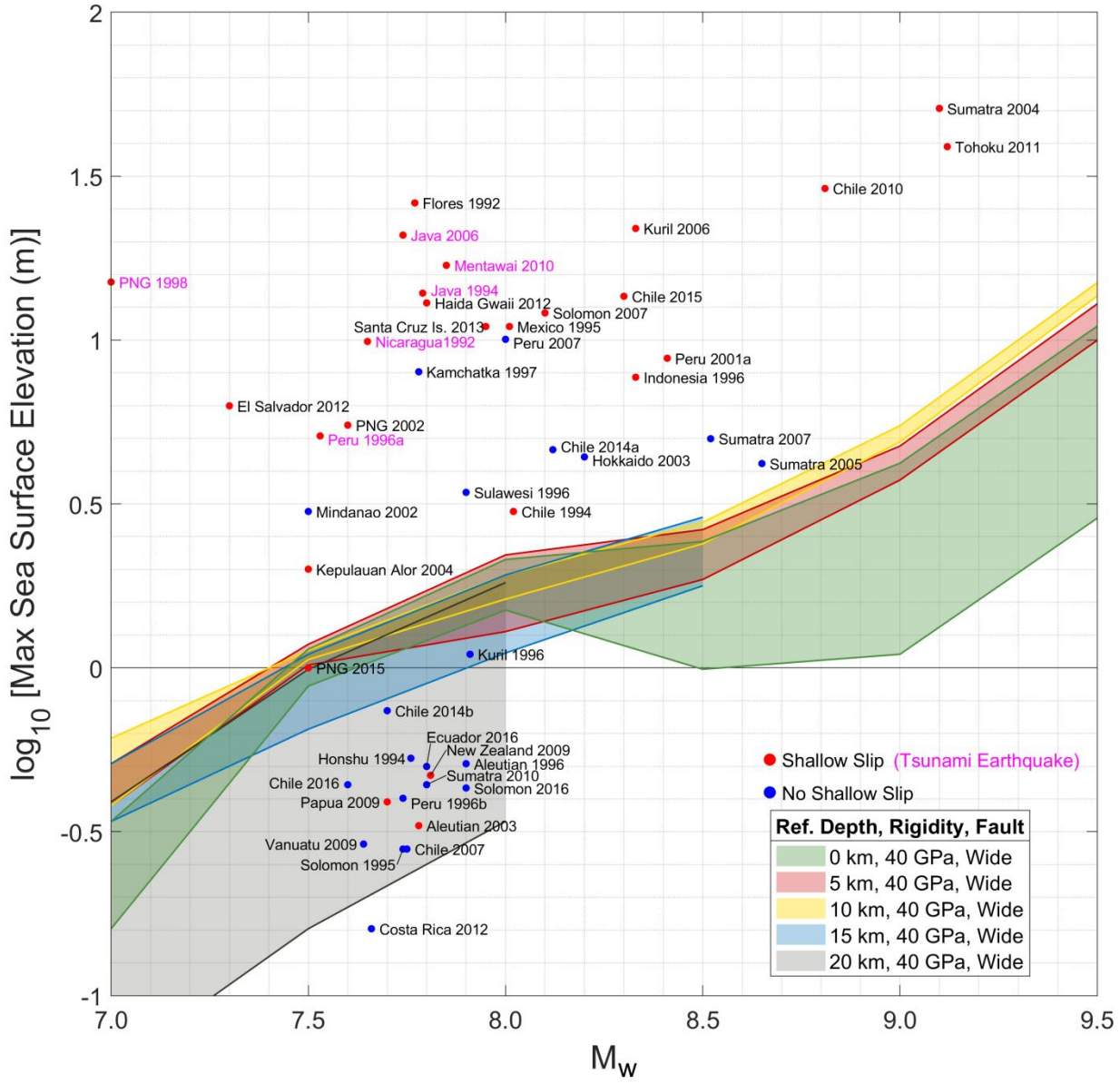


**Figure 27.** Comparison of computed peak surge from the wide fault and the recorded maximum sea surface elevation compiled by Lay et al. (2019) in terms of moment magnitude and reference depth. Color bands represent peak surge computed for 5° to 25° dip angle. PNG stands for Papua New Guinea.

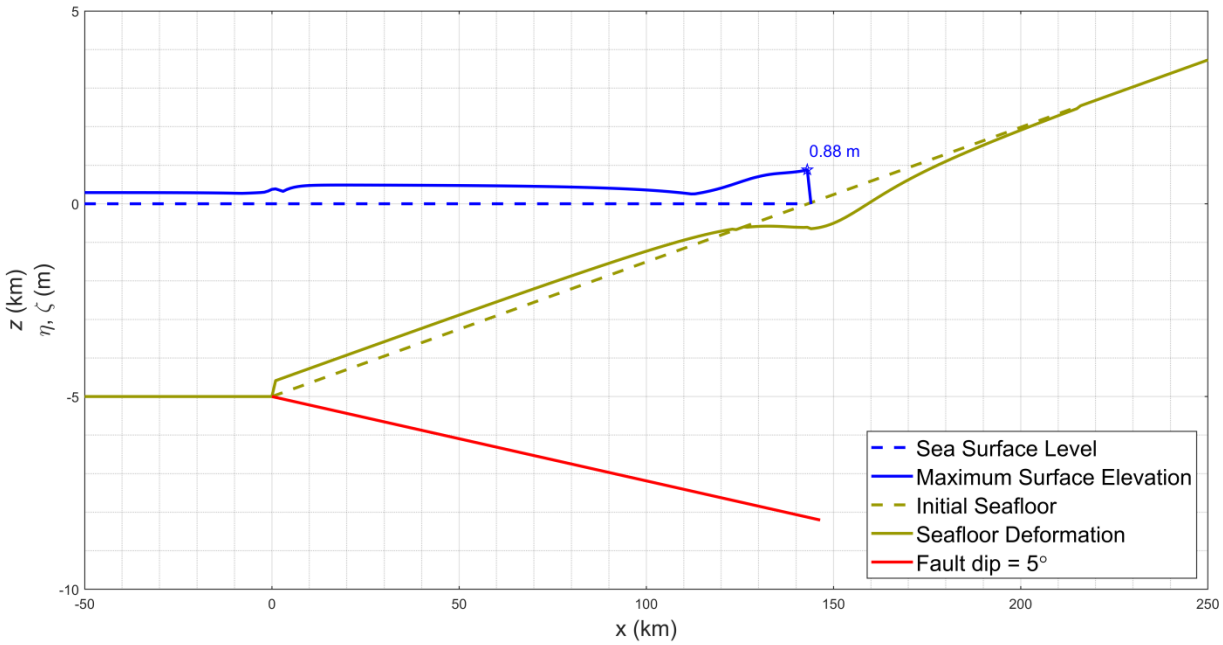


**Figure 28.** Maximum seafloor displacement and sea surface elevation as a function of x for Mw.

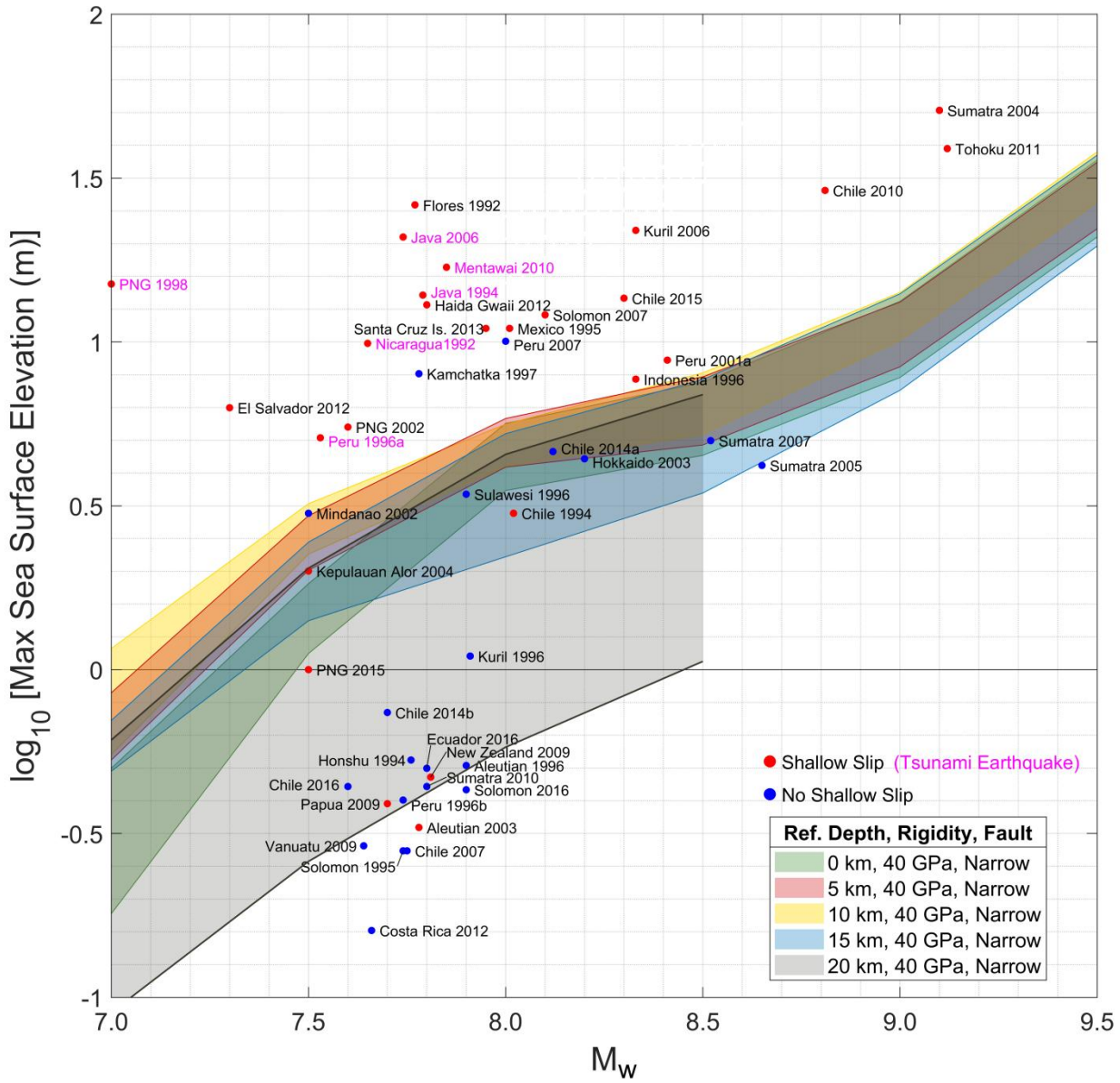


**Figure 29.** Comparison of computed peak surge by from the narrow fault and the recorded maximum sea surface elevation compiled by Lay et al. (2019) in terms of moment magnitude and reference depth. Color bands represent peak surge computed for 5° to 25° dip angle. PNG stands for Papua New Guinea.

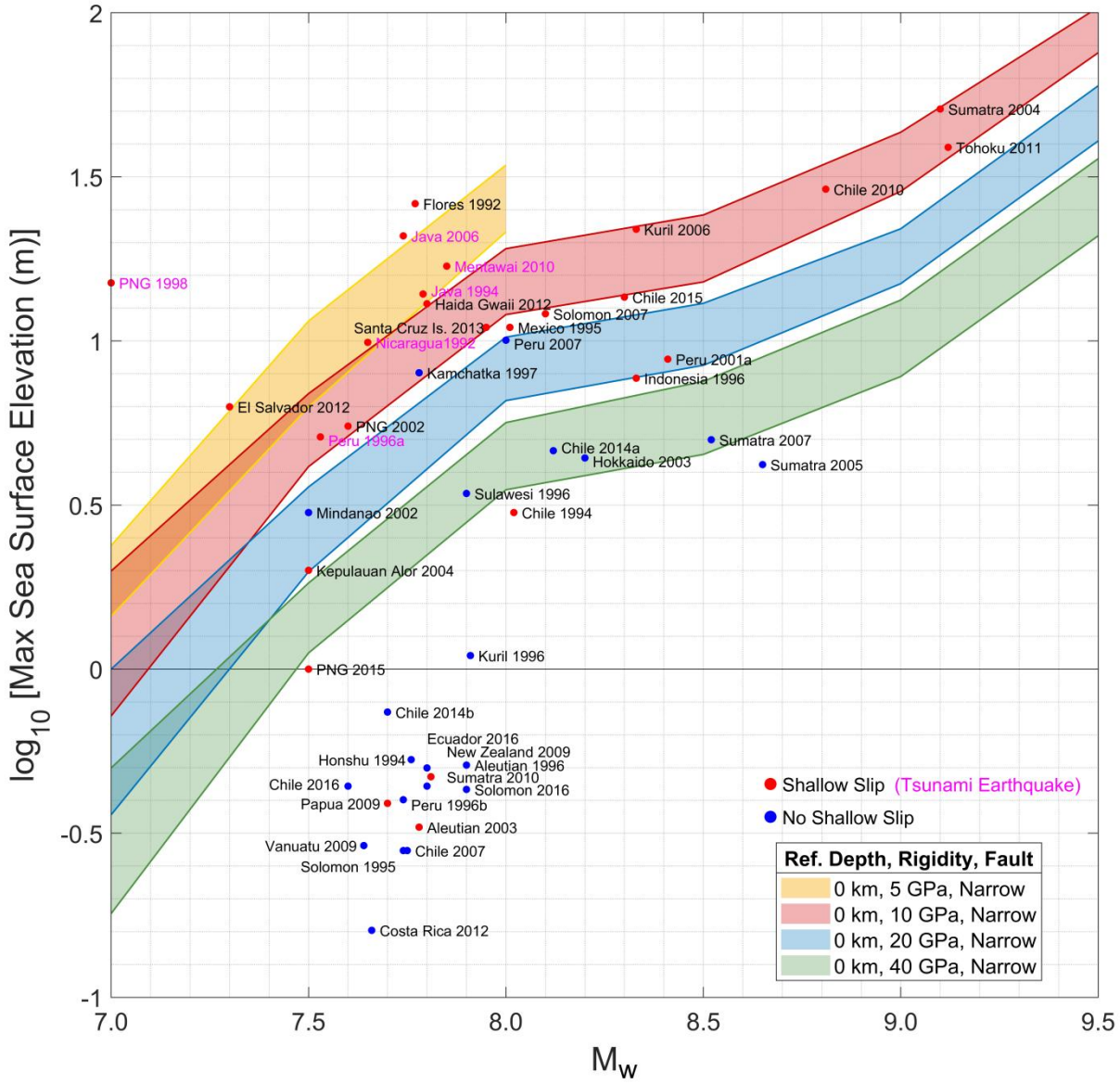


**Figure 30.** Comparison of computed peak surge by from the narrow fault and the recorded maximum sea surface elevation compiled by Lay et al. (2019) in terms of moment magnitude and source region rigidity. Color bands represent peak surge computed for 5° to 25° dip angle. PNG stands for Papua New Guinea.

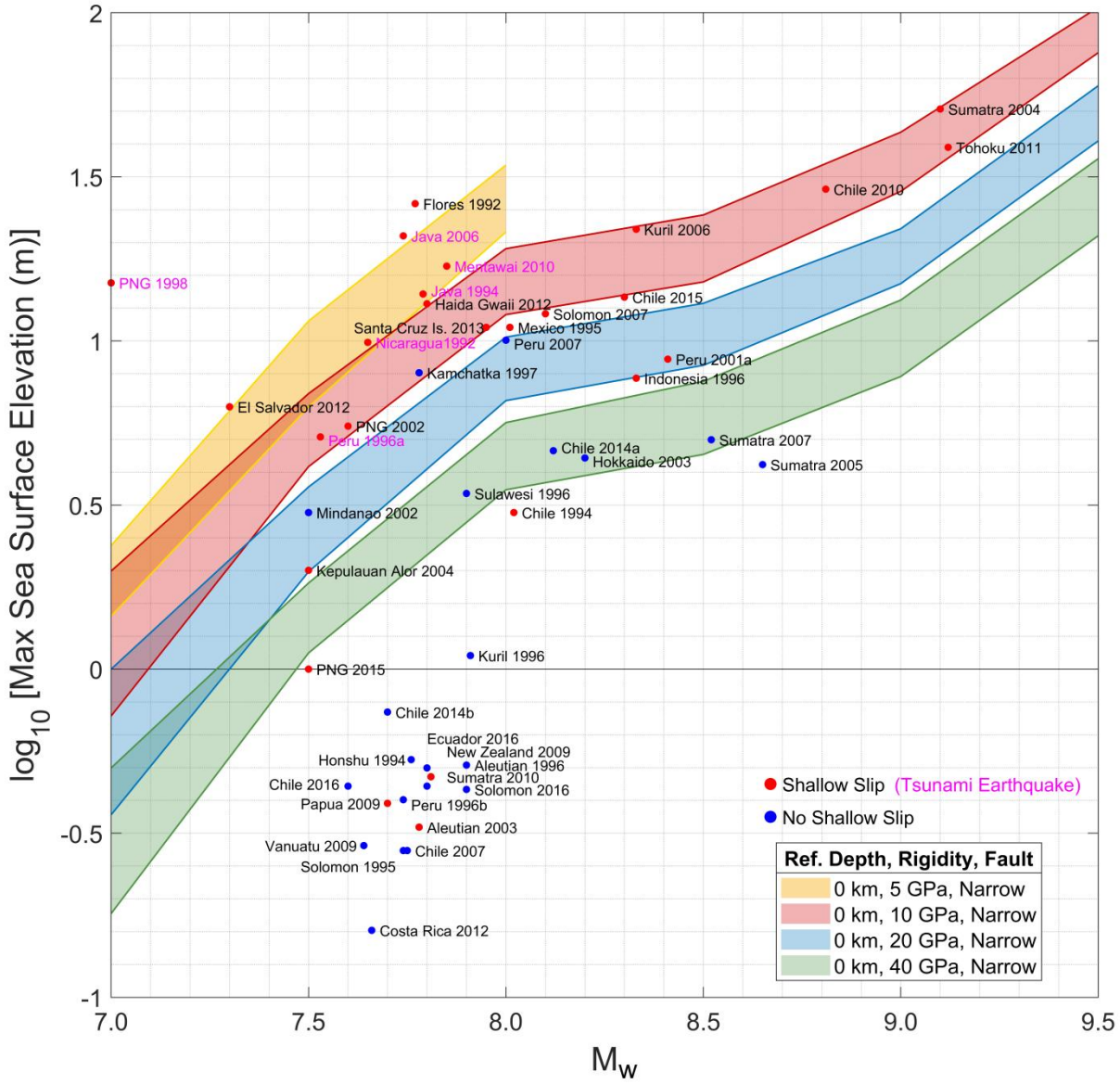


**Figure 31.** Selected computed maximum surge from Figures 26, 28, 29 and the recorded maximum sea surface elevation as functions of earthquake moment magnitude (Mw). Color bands represent peak surge computed for 5° to 25° dip angle. PNG stands for Papua New Guinea.

# References


Aki, K. (1966). Generation and Propagation of G Waves from the Niigata Earthquake of June 16, 1964.: Part 2. Estimation of earthquake moment, released energy, and stress-strain drop from the G wave spectrum. Bulletin of the Earthquake Research Institute, University of Tokyo, 44(1), 73-88.

Abe, K. (1979). Size of great earthquakes of 1837–1974 inferred from tsunami data. Journal of Geophysical Research: Solid Earth, 84(B4), 1561-1568.

Abe, K. (1981). Physical size of tsunamigenic earthquakes of the northwestern Pacific. Physics of the Earth and Planetary Interiors, 27(3), 194-205.

Abe, K. (1994). Instrumental magnitudes of historical earthquakes, 1892 to 1898. Bulletin of the Seismological Society of America, 84(2), 415-425.

Allen, R. M., & Ziv, A. (2011). Application of real-time GPS to earthquake early warning. Geophysical Research Letters, 38(16), doi: 10.1029/2011GL047947

Allen, T. I., & Hayes, G. P. (2017). Alternative rupture-scaling relationships for subduction interface and other offshore environments. Bulletin of the Seismological Society of America, 107(3), 1240-1253.

Ammon, C., Kanamori, H., Lay, T., & Velasco, A. (2006). The 17 July 2006 Java tsunami earthquake. Geophysical Research Letters, 33(24), doi: 10.1029/2006GL028005 ,

Bai, Y., Yamazaki, Y., & Cheung, K.F. (2015). NEOWAVE. Proceedings and Results of the 2015 National Tsunami Hazard Mitigation Program Model Benchmarking Workshop, Portland, Oregon, pp. 165–177.

Barré de Saint-Venant, A. J. (1856). Mémoire sur la torsion des prismes. Journal de Mathématique, 2(1).

Bilek, S. L., & Lay, T. (1999). Rigidity variations with depth along interplate megathrust faults in subduction zones. Nature, 400(6743), 443-446.

Blewitt, G., Kreemer, C., Hammond, W., Plag, H., Stein, S., & Okal, E. (2006). Rapid determination of earthquake magnitude using GPS for tsunami warning systems. Geophysical Research Letters, 33(11), doi: 10.1029/2006GL026145

Brengman, C. M., Barnhart, W. D., Mankin, E. H., & Miller, C. N. (2019). Earthquake-scaling relationships from geodetically derived slip distributions. Bulletin of the Seismological Society of America, 109(5), 1701-1715.

Fritz, H. M., Kongo, W., Moore, A., McAdoo, B., Goff, J., Harbitz, C., Uslu, B., Kalligeris, N., Suteja, D., Kalsum, K., Titov, V., Gusman, A., Latief, H., Santoso, E., Sujoko, S., Djulkarnaen, D., Sunendar, H., Synolakis, C. (2007). Extreme runup from the 17 July 2006 tsunami, Geophysical Research Letters, 34 (12), L12602, doi: 10.1029/2007gl029404.

Fuentes, M., Riquelme, S., Hayes, G., Medina, M., Melgar, D., Vargas, G., … Villalobos, A. (2016). A Study of the 2015 M w 8.3 Illapel Earthquake and Tsunami: Numerical and Analytical Approaches. Pure and Applied Geophysics, 173(6), 1847–1858, doi: 10.1007/s00024-016-1305-0

Fujii, Y., Satake, K., Sakai, S. I., Shinohara, M., & Kanazawa, T. (2011). Tsunami source of the 2011 off the Pacific coast of Tohoku Earthquake. Earth, Planets and Space, 63(7), 815-820, doi:10.5047/eps.2011.06.010.

Gusman, A., Satake, K., Shinohara, M., Sakai, S., & Tanioka, Y. (2017). Fault Slip Distribution of the 2016 Fukushima Earthquake Estimated from Tsunami Waveforms. Pure and Applied Geophysics, 174(8), 2925–294, doi: org/10.1007/s00024-017-1590-2

G. Gutenberg and C. F. Richter: Seismicity of the earth and associated phenomena. (1950). Journal of Geophysical Research, 55(1), 97–98, doi: 10.1029/JZ055i001p00097

Hayes, G. P., Benz, H. M., & Barnhart, W. D. (2015). Near realtime, multi-approach earthquake source inversion, and an extensive, consistent finite fault database. Seismol. Res. Lett., (2B), 711.

Hayes, G. (2017). The finite, kinematic rupture properties of great-sized earthquakes since 1990. Earth and Planetary Science Letters, 468, 94–100, doi:10.1016/j.epsl.2017.04.003.

Hidayat, D., Barker, J. S., & Satake, K. (1995). Modeling the seismic source and tsunami generation of the December 12, 1992 Flores Island, Indonesia, earthquake. pure and applied geophysics, 144(3-4), 537-554.

Hill, E., Borrero, J., Huang, Z., Qiu, Q., Banerjee, P., Natawidjaja, D., … Sieh, K. (2012). The 2010 Mw 7.8 Mentawai earthquake : very shallow source of a rare tsunami earthquake determined from tsunami field survey and near-field GPS data. Journal of Geophysical Research: Solid Earth, 117, B06402, doi: 10.1029/2012JB009159.

Huang, P., Whitmore, P., Johnson, P., Bahng, B., Burgy, M., Cottingham, T., Gately, K., Goosby, S., Hale, D., Yoo Yin Kim, Langley, S., Macpherson, K., Ohlendorf, S., Popham, C., Rasch, R., Varnado, C., Varnado, L., & Waddell, J. (2017). Real-time earthquake monitoring and tsunami warning operations at the U.S. National Tsunami Warning Center. OCEANS 2017 - Anchorage, 1–6.

Iwasaki, S., & Iwasaki, S. (1982). Experimental study of a tsunami generated by a horizontal motion of a sloping bottom. Bulletin of the Earthquake Research Institute, University of Tokyo, 57, 239–262.

Johnson, J. M., & Satake, K. (1997). Estimation of seismic moment and slip distribution of the April 1, 1946, Aleutian tsunami earthquake. Journal of Geophysical Research: Solid Earth, 102(B6), 11765-11774.

Kajiura, K., & Kajiura, K. (1981). Tsunami energy in relation to parameters of the earthquake fault model. Bulletin of the Earthquake Research Institute, University of Tokyo, 56, 415–440.

Kanamori, H. (1972). Mechanism of tsunami earthquakes. Physics of the Earth and Planetary Interiors, 6(5), 346–359, doi: 10.1016/0031-9201(72)90058-1.

Kanamori, H. (1977). The energy release in great earthquakes. Journal of Geophysical Research, 82(20), 2981-2987.

Kanamori, H. (1993). W phase. Geophysical research letters, 20(16), 1691-1694.

Kanamori, H., & Rivera, L. (2008). Source inversion ofWphase: speeding up seismic tsunami warning. Geophysical Journal International, 175(1), 222-238.

Lay, T., Ammon, C., Kanamori, H., Yamazaki, Y., Cheung, K., & Hutko, A. (2011). The 25 October 2010 Mentawai tsunami earthquake (M w 7.8) and the tsunami hazard presented by shallow megathrust ruptures. Geophysical Research Letters, 38(6), doi: 10.1029/2010GL046552.

Lay, T., Kanamori, H., Ammon, C., Koper, K., Hutko, A., Ye, L., … Rushing, T. (2012). Depth-varying rupture properties of subduction zone megathrust faults. Journal of Geophysical Research: Solid Earth, 117(B4), doi: 10.1029/2011JB009133.

Lay, T., Liu, C., & Kanamori, H. (2019). Enhancing Tsunami Warning Using P Wave Coda. Journal of Geophysical Research: Solid Earth, 124(10), 10583–10609, doi: 10.1029/2019JB018221.

Lay, T. (2018). A review of the rupture characteristics of the 2011 Tohoku-oki Mw 9.1 earthquake. Tectonophysics, 733, 4-36.

Li, L., Cheung, K., Yue, H., Lay, T., & Bai, Y. (2016). Effects of dispersion in tsunami Green's functions and implications for joint inversion with seismic and geodetic data: A case study of the 2010 Mentawai Mw 7.8 earthquake. Geophysical Research Letters, 43(21), 11,182–11,191, doi: 10.1002/2016GL070970.

Liu, C., Zheng, Y., Xiong, X., Wang, R., López, A and Li, J. (2015). Rupture processes of the 2012 September 5 M w 7.6 Nicoya, Costa Rica earthquake constrained by improved geodetic and seismological observations. Geophysical Journal International, 203(1), 175-183.

Loomis, G.H. (1976). Tsunami Wave Runup Heights in Hawaii. Hawaii Institute of Geophysics, University of Hawaii, Honolulu, Hawaii.

Mayu Inoue, Yuichiro Tanioka, & Yusuke Yamanaka. (2019). Method for Near-Real Time Estimation of Tsunami Sources Using Ocean Bottom Pressure Sensor Network (S-Net). Geosciences (Basel), 9(7), doi: 10.3390/geosciences9070310.

Mochizuki, M., Uehira, K., Kanazawa, T., Kunugi, T., Shiomi, K., Aoi, S., Matsumoto, T., Takahashi, N., Chikasada, N., Nakamura, T., Sekiguchi, S., Shinohara, M., & Yamada, T. (2018). S-Net project: Performance of a Large-Scale Seafloor Observation Network for Preventing and Reducing Seismic and Tsunami Disasters. 2018 OCEANS - MTS/IEEE Kobe Techno-Oceans (OTO), 1–4, doi: 10.1109/OCEANSKOBE.2018.8558823.

Moore, G. F., Bangs, N. L., Taira, A., Kuramoto, S., Pangborn, E., & Tobin, H. J. (2007). Three-dimensional splay fault geometry and implications for tsunami generation. Science, 318(5853), 1128-1131.

Mori, N., Takahashi, T., Yasuda, T., & Yanagisawa, H. (2011). Survey of 2011 Tohoku earthquake tsunami inundation and run-up. Geophysical Research Letters, 38, L00G14, doi: 10.1029/2011GL049210.

Newman, A., Hayes, G., Wei, Y., & Convers, J. (2011). The 25 October 2010 Mentawai tsunami earthquake, from real-time discriminants, finite-fault rupture, and tsunami excitation. Geophysical Research Letters, 38(5), doi: 10.1029/2010GL046498.

Okada, Y. (1985). Surface deformation due to shear and tensile faults in a half-space. Bulletin of the Seismological Society of America, 75(4), 1135–1154.

Okal, E. A. (1988). Seismic parameters controlling far-field tsunami amplitudes: A review. Natural Hazards, 1(1), 67-96.

Okal, E.A., & Hébert, H. (2007). Far-field tsunami simulation of the 1946 Aleutian tsunami. Geophysical Journal International, 169(3), 1229-1238.

Segall, P., & Davis, J. L. (1997). GPS applications for geodynamics and earthquake studies. Annual Review of Earth and Planetary Sciences, 25(1), 301-336.

Saito, T. (2013). Dynamic tsunami generation due to sea-bottom deformation: Analytical representation based on linear potential theory. Earth, Planets and Space, 65(12), 1411–1423, doi: 10.5047/eps.2013.07.004.

Satake, K., Fujii, Y., & Yamaki, S. (2017). Different depths of near-trench slips of the 1896 Sanriku and 2011 Tohoku earthquakes. Geoscience Letters, 4(1), 1–10, doi: 10.1186/s40562-017-0099-y.

Shao, G., Li, X., Ji, C., & Maeda, T. (2011). Focal mechanism and slip history of the 2011 M w 9.1 off the Pacific coast of Tohoku Earthquake, constrained with teleseismic body and surface waves. Earth, planets and space, 63(7), 559-564.

Steketee, J. (1958). On Volterra's Dislocation A Semi-Infinite Elastic Medium. Canadian Journal of Physics, 36(2), 192–205, doi: 10.1139/p58-024.

Synolakis, C. E., Bardet, J. P., Borrero, J. C., Davies, H. L., Okal, E. A., Silver, E. A., ... & Tappin, D. R. (2002). The slump origin of the 1998 Papua New Guinea tsunami. Proceedings of the Royal Society of London. Series A: Mathematical, Physical and Engineering Sciences, 458(2020), 763-789.

Tanioka, Y., & Sataka, K. (1996a). Fault parameters of the 1896 Sanriku tsunami earthquake estimated from tsunami numerical modeling. Geophysical Research Letters, 23(13), 1549-1552.

Tanioka, Y., & Satake, K. (1996b). Tsunami generation by horizontal displacement of ocean bottom. Geophysical Research Letters, 23(8), 861–864, doi: 10.1029/96GL00736.

Tanioka, Y., Ruff, L., & Satake, K. (1997). What controls the lateral variation of large earthquake occurrence along the Japan Trench. Island Arc, 6(3), 261-266.

Titov, V. V., Gonzalez, F. I., Bernard, E. N., Eble, M. C., Mofjeld, H. O., Newman, J. C., & Venturato, A. J. (2005). Real-time tsunami forecasting: Challenges and solutions. Natural Hazards, 35(1), 35-41.

Titov, V., Kânoğlu, U., & Synolakis, C. (2016). Development of MOST for Real-Time Tsunami Forecasting. Journal of Waterway, Port, Coastal, and Ocean Engineering, 142(6), 1–16, doi: 10.1061/(ASCE)WW.1943-5460.0000357

Tsuboi, S., Abe, K., Takano, K., & Yamanaka, Y. (1995). Rapid determination of Mw from broadband P waveforms. Bulletin of the Seismological Society of America, 85(2), 606-613.

Tsuru, T., Park, J. O., Takahashi, N., Kodaira, S., Kido, Y., Kaneda, Y., & Kono, Y. (2000). Tectonic features of the Japan Trench convergent margin off Sanriku, northeastern Japan, revealed by multichannel seismic reflection data. Journal of Geophysical Research: Solid Earth, 105(B7), 16403-16413.

USACE. (2006). Coastal Engineering Manual. U.S. Army Corps of Engineers, Washington, D.C.

Wang, D., Becker, N., Walsh, D., Fryer, G., Weinstein, S., Mccreery, C., Sardiña, V., Hsu, V., Hirshorn, B., Hayes, G., Duputel, Z., Rivera, L., Kanamori, H., Koyanagi, K., & Shiro, B. (2012). Real-time forecasting of the April 11, 2012 Sumatra tsunami. Geophysical Research Letters, 39(19), n/a–n/a, doi: 10.1029/2012GL053081

Wang, D., Becker, N. C., Weinstein, S., Duputel, Z., Rivera, L. A., Hayes, G. P., ... & Mungov, G. (2017, December). Evaluation of W Phase CMT Based PTWC Real-Time Tsunami Forecast Model Using DART Observations: Events of the Last Decade. In 2017 AGU Fall Meeting. AGU.

Weinstein, S. A., & Okal, E. A. (2005). The mantle magnitude Mm and the slowness parameter θ: five years of real-time use in the context of tsunami warning. Bulletin of the Seismological Society of America, 95(3), 779-799.

Wells, D., & Coppersmith, K. (1994). New empirical relationships among magnitude, rupture length, rupture width, rupture area, and surface displacement. Bulletin of the Seismological Society of America, 84(4), 974–1002.

Yamazaki, Y., Kowalik, Z., & Cheung, K. (2009). Depth-integrated, non-hydrostatic model for wave breaking and run-up. International Journal for Numerical Methods in Fluids, 61(5), 473–497. https://doi.org/10.1002/fld.1952.

Yamazaki, Y., Cheung, K., & Kowalik, Z. (2011). Depth-integrated, non-hydrostatic model with grid nesting for tsunami generation, propagation, and run-up. International Journal for Numerical Methods in Fluids, 67(12), 2081–2107, doi: 10.1002/fld.2485.

Yamazaki, Y., Cheung, K.F., Kowalik, Z., Pawlak, G., & Lay, T. (2012). NEOWAVE. Proceedings and Results of the 2011 National Tsunami Hazard Mitigation Program, Model Benchmarking Workshop, Galveston, Texas, pp. 239–302.

Yamazaki, Y., Cheung, K., & Lay, T. (2018). A Self-Consistent Fault Slip Model for the 2011 Tohoku Earthquake and Tsunami. Journal of Geophysical Research: Solid Earth, 123(2), 1435–1458, doi: 10.1002/2017JB014749**.**

Ye, L., Lay, T., Kanamori, H., & Rivera, L. (2016). Rupture characteristics of major and great (Mw $\geq$ 7.0) megathrust earthquakes from 1990 to 2015: 1. Source parameter scaling relationships. Journal of Geophysical Research: Solid Earth, 121(2), 826–844, doi: 10.1002/2015JB012426

Yoshihiro Kaneko, Jean-Philippe Avouac, & Nadia Lapusta. (2010). Towards inferring earthquake patterns from geodetic observations of interseismic coupling. Nature Geoscience, 3(5), 363–369, doi: 10.1038/ngeo843.

Yue, H., Lay, T., Rivera, L., Bai, Y., Yamazaki, Y., Cheung, K., … Muhari, A. (2014). Rupture process of the 2010 Mw 7.8 Mentawai tsunami earthquake from joint inversion of near-field

hr-GPS and teleseismic body wave recordings constrained by tsunami observations. Journal of Geophysical Research: Solid Earth, 119(7), 5574–5593, doi: 10.1002/2014JB011082.